



저작자표시-비영리-변경금지 2.0 대한민국

이용자는 아래의 조건을 따르는 경우에 한하여 자유롭게

- 이 저작물을 복제, 배포, 전송, 전시, 공연 및 방송할 수 있습니다.

다음과 같은 조건을 따라야 합니다:



저작자표시. 귀하는 원저작자를 표시하여야 합니다.



비영리. 귀하는 이 저작물을 영리 목적으로 이용할 수 없습니다.



변경금지. 귀하는 이 저작물을 개작, 변형 또는 가공할 수 없습니다.

- 귀하는, 이 저작물의 재이용이나 배포의 경우, 이 저작물에 적용된 이용허락조건을 명확하게 나타내어야 합니다.
- 저작권자로부터 별도의 허가를 받으면 이러한 조건들은 적용되지 않습니다.

저작권법에 따른 이용자의 권리는 위의 내용에 의하여 영향을 받지 않습니다.

이것은 [이용허락규약\(Legal Code\)](#)을 이해하기 쉽게 요약한 것입니다.

[Disclaimer](#)

공학박사 학위논문

***n*-Doping of Electron Transporting
Layer for High Performance
Perovskite Solar Cells with Planar
Heterojunction Architecture**

평면 이종접합 구조를 갖는

고성능의 페로브스카이트 태양전지를 위한

전자 수송층의 *n*-도핑

2016년 2월

서울대학교 대학원

재료공학부

김 신 성

Abstract

***n*-Doping of Electron Transporting
Layer for High Performance
Perovskite Solar Cells with Planar
Heterojunction Architecture**

Shin Sung Kim

Department of Materials Science and Engineering

The Graduate School

Seoul National University

Organic-inorganic hybrid perovskite has intensively been studied as light absorber for efficient photovoltaic cells because of its unique and superior intrinsic properties such as long charge carrier diffusion length, excellent charge carrier transport, low exciton binding energy, and high absorption coefficient. Furthermore, thin films of organic-inorganic perovskites can be easily fabricated from abundant and inexpensive precursor materials. In spite of their short history, the photovoltaic performances of perovskite solar cells have advanced dramatically with surpassing a power conversion efficiency (PCE) of 20%.

Particularly, inverted structure of planar heterojunction perovskite solar cell with a device configuration of ITO/PEDOT:PSS/perovskite($\text{CH}_3\text{NH}_3\text{PbI}_3$)/electron transporting material/Al has attracted much attention due to an advantage of low-temperature and solution processibility over the normal

structure. For inverted perovskite solar cells, fullerene derivatives such as C₆₀, PCBM, PC₇₁BM, and ICBA have commonly been used as electron transporting layer (ETL) material because of their room temperature solubility and orthogonal solvent processibility on the perovskite layer.

In organic photovoltaics, non-fullerene electron acceptors based on polymers and small molecules have recently been developed because of their unique advantages over fullerene derivatives such as high absorption in visible range, tunable energy level, and low production cost. However, since inverted perovskite solar cells require sufficiently thick ETL to prevent direct contact between perovskite layer and metal cathode, the non-fullerene acceptors as ETL material of perovskite solar cells must have sufficiently high electrical conductivity and high electron mobility.

1,3-Dimethyl-2-phenyl-2,3-dihydro-1*H*-benzoimidazole (DMBI) has been reported as an effective *n*-type dopant for enhancing the electrical properties of *n*-type materials such as fullerene or naphthalene diimide derivatives. Since DMBI has good solubility in common organic solvents, the doping is easily achieved by simply mixing with *n*-type material in organic solvents. DMBI is expected to effectively dope the electron transporting materials and thus to enhance the solar cell performance of planar heterojunction perovskite solar cells.

In this study, a simple *n*-doping method to enhance the performance of *n*-type materials as electron transporting layer of perovskite solar cells with planar heterojunction architecture is investigated. *n*-Type materials used in this study are PCBM and perylene diimide-based small molecules. When a small amount of DMBI is added to ETL materials, it reveals that DMBI effectively dopes the ETL as clearly evidenced by up-shift of the Fermi level. Further, the device with DMBI-doped ETL exhibits high PCE with remarkably enhanced short-circuit current density as compared to the device with undoped ETL, mainly due to the greatly increased electrical conductivity

of ETL materials. When the charge transfer characteristics are identified by photoluminescence measurements, it reveals that the electron accepting ability of diPDI is comparable to that of PCBM.

Keywords: perovskite solar cells, planar heterojunction, inverted structure, *n*-doping, electron transporting layer, charge transport, electrical conductivity, non-fullerene acceptor

Student Number: 2010-24052

Contents

Chapter 1 Introduction	1
1.1 Organic-inorganic hybrid perovskite solar cells	1
1.1.1 Organic-inorganic hybrid perovskites.....	1
1.1.2 Advantages of organic-inorganic hybrid perovskites as solar cell materials	5
1.1.2.1 Charge carrier diffusion lengths.....	6
1.1.2.2 Charge carrier mobility	8
1.1.2.3 Exciton binding energy	8
1.1.2.4 Optical properties.....	10
1.1.3 Classification by device structure	13
1.1.4 Fabrication methods for organic-inorganic hybrid perovskite films	16
1.2 Planar heterojunction perovskite solar cells with inverted device configuration.....	19
1.2.1 Operating principles.....	19
1.2.2 Device structure	22
1.2.3 <i>n</i> -Doping method	26
1.2.4 Non-fullerene electron acceptors	29
1.3 Objectives of this study.....	33
Chapter 2 Experimental Section.....	36
2.1 Synthesis and characterization.....	36
2.1.1 Materials	36
2.1.2 Synthesis of organic precursor of perovskite films.....	37
2.1.3 Fabrication of perovskite films	38
2.1.4 Synthesis of titanium dioxide nanoparticles	39
2.1.5 Synthesis of <i>n</i> -type dopant.....	39
2.1.6 Synthesis of non-fullerene acceptors	41
2.1.6.1 Synthesis of <i>N,N'</i> -bis(1-propylbutyl)perylene-3,4:9,10-tetracarboxylic diimide	41

2.1.6.2	Synthesis of 1-bromo- <i>N,N'</i> -bis(1-propylbutyl)perylene-3,4:9,10-tetracarboxylic diimide	41
2.1.6.3	Synthesis of diPDI	42
2.1.7	Characterization methods.....	42
2.2	Device fabrication and measurements	44
2.2.1	Materials	44
2.2.2	Fabrication of solar cell devices.....	45
2.2.2.1	Fabrication of solar cell devices with PCBM ETL ..	45
2.2.2.2	Fabrication of solar cell device with non-fullerene ETL	46
2.2.3	Solar cell performance measurements	46

Chapter 3 Results and Discussion.....48

3.1	Performance enhancement of inverted structure planar heterojunction perovskite solar cells by <i>n</i> -doping of PCBM electron transporting layer	48
3.1.1	Synthesis and characterization	48
3.1.2	Characterization of <i>n</i> -doping	50
3.1.3	Photovoltaic properties	54
3.1.4	Effects of excessive doping on photovoltaic properties.....	60
3.1.5	Summary	65
3.2	Perylene diimide-based non-fullerene acceptors as electron transporting materials for inverted structure planar heterojunction perovskite solar cells and the performance enhancement by <i>n</i> -doping	67
3.2.1	Synthesis and characterization	67
3.2.2	Charge transfer characteristics	69
3.2.3	Photovoltaic properties	72
3.2.4	Characterization of <i>n</i> -doping	76
3.2.5	Effects of excessive doping on photovoltaic properties.....	79
3.2.6	PDI monomer as ETL material	82
3.2.7	Summary	86

Chapter 4 Conclusions	89
Bibliography	93
Korean Abstract	103

List of Tables

Table 3.1	The best photovoltaic properties of devices with PCBM ETL with different thickness and different dopant concentrations	57
Table 3.2	Average device parameters and their standard deviations based on at least 10 devices.	59
Table 3.3	Fitting parameters of PL decays shown in Figure 3.10	65
Table 3.4	Fitting parameters of PL decays shown in Figure 3.15	72
Table 3.5	Photovoltaic performances of devices with diPDI with different dopant (DMBI) concentrations as ETL.....	75
Table 3.6	Fitting parameters of PL decays shown in Figure 3.21	82
Table 3.7	Photovoltaic performances of devices with PDI with different dopant (DMBI) concentrations as ETL.....	84

List of Schemes

Scheme 2.1	Synthetic scheme of DMBI.....	40
Scheme 2.2	Synthetic scheme of diPDI	40

List of Figures

Figure 1.1	Crystal structure of perovskites (ABX_3)..... 2
Figure 1.2	Perovskite distortion from (a) cubic to (b) orthorhombic..... 3
Figure 1.3	Schematic representation of the basic structures of two-dimensional organic-inorganic perovskites with (a) bilayer and (b) single layer intercalated organic molecules. (Ref. 2) . 4
Figure 1.4	(A) Time-integrated photoluminescence (PL) spectra and (B) Time-resolved PL decay transients measured at 760 ± 10 nm for quartz/ $CH_3NH_3PbI_3$ (65 nm) (black), quartz/ $CH_3NH_3PbI_3$ (65 nm)/PCBM (red), quartz/ $CH_3NH_3PbI_3$ (65 nm)/spiro-OMeTAD (blue) films in vacuum after excitation at 600 nm. The solid lines in (B) are the single-exponential fits of the PL decay transients. (C) A plot of exciton diffusion length versus PL lifetime quenching ratios. Diffusion length is scaled in multiples of $CH_3NH_3PbI_3$ layer thickness ($L = 65$ nm). (Ref. 25). 7
Figure 1.5	Carrier mobility characterization of $CH_3NH_3PbI_3$ single crystal. Current-voltage curve for (A) a hole-only device and (B) an electron-only device. The insets show the device structure of hole-only and electron-only devices, respectively. (C) Schematic illustration of the device for the time-of-flight measurement. (D) The transient current curves of the $CH_3NH_3PbI_3$ single crystal device show the normalized transient photocurrent under various reverse biases. (Ref. 19)9
Figure 1.6	(a) Absorption coefficient of $CH_3NH_3PbI_3$ and $CH_3NH_3PbI_{3-x}Cl_x$ compared to other solar cell materials. (b) Real and imaginary parts of the $CH_3NH_3PbI_3$ dielectric constant at 300 K as a function of frequency. (Ref. 9)..... 11
Figure 1.7	(a) UV-Vis absorbance of the $FAPbI_{1-y}Br_y$ perovskites with varying y. (b) Corresponding steady-state photoluminescence spectra for the same films. (c) Photographs of the $FAPbI_{1-y}Br_y$ perovskite films with y increasing from 0 to 1 (left to right). (Ref. 12). 12

Figure 1.8	(a) Cross-sectional scanning electron microscope image of solid-state DSSC structure. (b) Schematic illustration of charge transfer in mesoscopic type perovskite solar cells and the energy levels of TiO_2 , $\text{CH}_3\text{NH}_3\text{PbI}_3$, and spiro-OMeTAD... 14
Figure 1.9	Schematic representation of the charge transfer and charge transport in a perovskite-sensitized TiO_2 solar cell and a noninjecting Al_2O_3 -based solar cell. (Ref. 31)..... 15
Figure 1.10	(a) Schematic representation of the dual-source thermal evaporation system for depositing the perovskite absorbers; the organic source is methylammonium iodide and the inorganic source is PbCl_2 . (b) X-ray diffraction spectra of a solution-processed perovskite film (blue) and vapor-deposited perovskite film (red). (c) SEM top view of a vapor-deposited perovskite film. (d) SEM top view of a solution-processed perovskite film. (Ref. 32)..... 17
Figure 1.11	Schematic representation of solvent engineering procedure and SEM image of perovskite film fabricated by solvent engineering process. (Ref. 33). 18
Figure 1.12	Fundamental operating principles of solar cells. (Ref. 36).... 20
Figure 1.13	Current density voltage curves of solar cells under illumination and in the dark. The photovoltaic parameters are represented. 21
Figure 1.14	Schematic representation of device structure of planar heterojunction perovskite solar cells with (a) normal and (b) inverted configuration. 23
Figure 1.15	Energy levels of each layer of device with inverted planar heterojunction structure. (Ref. 39)..... 24
Figure 1.16	Chemical structures of <i>n</i> -type materials used as ETL materials for planar heterojunction perovskite solar cells with inverted device configuration. 25
Figure 1.17	(a) Conductivities of undoped and N-DMBI-dope dPCBM films at varying doping concentrations. Inset: AFM image of 2 wt% N-DMBI-doped PCBM film. (b) Transfer characteristics

	of N-DMBI-doped PCBM OTFTs at varying doping concentrations. (c) Output characteristics of 0.5 wt% N-DMBI-doped PCBM OTFTs. (d) Changes of field-effect mobilities in air as a function of time for undoped and 0.5 and 2 wt% N-DMBI-doped PCBM OTFTs. (Ref. 49).....	27
Figure 1.18	Energy level alignment of undoped and 1 wt% <i>o</i> -MeO-DMBI doped PC ₆₁ BM. (Ref. 51).....	28
Figure 1.19	Chemical structures of PDI or NDI-based polymer acceptors	30
Figure 1.20	(a) Chemical structures of polymer acceptor (PNDIS-HD) and donor polymer (PBDTT-FTTE). (b) Energy levels of the acceptor and donor materials. (c) Optical absorption spectra of the acceptor and donor materials. (Ref. 66).....	31
Figure 1.21	Chemical structures of PDI-based small molecule acceptors.	32
Figure 2.1	Schematic representation of perovskite film fabrication method.	38
Figure 3.1	¹ H NMR spectrum of methylammonium iodide.....	49
Figure 3.2	¹ H NMR spectrum of DMBI.	49
Figure 3.3	UV-Vis-NIR absorption spectra of pure PCBM film and DMBI-doped PCBM films with various doping concentrations. All films are fabricated by spin-coating the chloroform solution on glass.....	52
Figure 3.4	UPS spectra of pure PCBM and DMBI-doped PCBM with various doping concentrations for (a) high binding energy region and (b) low binding energy region. Binding energy cutoffs of PCBM and PCBM doped with 1 wt% DMBI are indicated.....	53
Figure 3.5	(a) Schematic of the device architecture used in this work. (b) Energy levels of each layer. Fermi levels (E_F) and HOMO energy levels of the ETL were determined for pure PCBM and 1 wt% doped PCBM by UPS measurements..	55
Figure 3.6	<i>J-V</i> curves of the devices with (a) a thin (50 nm) ETL which are fabricated by spin-coating of 10 mg mL ⁻¹ chloroform solution, and (b) a thick (105 nm) ETL which are fabricated by spin-coating of 20 mg mL ⁻¹ chloroform solution.....	56

Figure 3.7	EQE spectra of devices with (a) thin ETL and (b) thick ETL which are doped with various DMBI concentrations.. 58
Figure 3.8	AFM height images ($1 \mu\text{m} \times 1 \mu\text{m}$ scale) of (a) pure PCBM film, (b) 1wt%, (c) 3 wt%, (d) 5 wt%, and (e) 10 wt% DMBI-doped PCBM film.. 61
Figure 3.9	Hysteresis curves for devices with (a), (b), (c), (d) thin ETL, and (e), (f), (g), (h) thick ETL..... 62
Figure 3.10	Transient Photoluminescence spectra for perovskite/pure PCBM film, and perovskite/DMBI-doped PCBM films with various dopant concentrations deposited on quartz glass. 64
Figure 3.11	^1H NMR spectrum of PDI monomer (compound 2 in Scheme 2.2). 68
Figure 3.12	^1H NMR spectrum of mono-brominated PDI monomer (compound 3 in Scheme 2.2.). 68
Figure 3.13	^1H NMR spectrum diPDI. 69
Figure 3.14	Photoluminescence spectra for pristine perovskite, perovskite/diPDI, and perovskite/PCBM films deposited on quartz glass (excited at 520 nm). 70
Figure 3.15	Transient PL spectra for pristine perovskite, perovskite/diPDI, and perovskite/PCBM films deposited on quartz glass. 71
Figure 3.16	Energy levels of each layer of photovoltaic devices. 73
Figure 3.17	(a) $J-V$ curves, and (b) EQE spectra of the devices with pure diPDI and DMBI-doped diPDI with various dopant concentrations as ETL.. 74
Figure 3.18	UV-Vis-NIR absorption spectra of pure diPDI film and DMBI-doped diPDI films with various dopant concentrations. All films are fabricated by spin-coating the chlorobenzene solution on glass.. 77
Figure 3.19	UPS spectra of pure diPDI and DMBI-doped diPDI with various dopant concentrations in (a) high binding energy region and (b) low binding energy region. Binding energy cutoffs of pure diPDI and diPDI doped with 1 wt% DMBI are indicated..... 78
Figure 3.20	Hysteresis curves for devices with (a) pure diPDI, (b) 0.5

	wt% DMBI-doped diPDI, (c) 1 wt% DMBI-doped diPDI, (d) 3 wt% DMBI-doped diPDI, and (e) 5 wt% DMBI-doped diPDI.....	80
Figure 3.21	Transient Photoluminescence spectra for perovskite/pure diPDI film, and perovskite/DMBI-doped diPDI films with various dopant concentrations deposited on quartz glass... ..	81
Figure 3.22	(a) $J - V$ curves of the devices with pure PDI and DMBI-doped PDI with various dopant concentrations as ETL, and (b) comparison of device performance between diPDI and PDI monomer with un-doped and optimized (1 wt% of DMBI doped) devices.	83
Figure 3.23	Cyclic voltammograms of PDI monomer and diPDI.....	85

Chapter 1. Introduction

1.1 Organic-inorganic hybrid perovskite solar cells

1.1.1 Organic-inorganic hybrid perovskites

A perovskite is any material with the same type of crystal structure as calcium titanium oxide (CaTiO_3), known as the perovskite structure. The CaTiO_3 mineral was first discovered in the Ural Mountains by Gustav Rose in 1839, and is named after Russian mineralogist Lev Perovski. The perovskite crystal structure was first described by Victor Goldschmidt in 1926. The compounds of perovskite family exist extensively in nature, and some researchers believe that magnesium silicate perovskite (MgSiO_3) is the most abundant mineral in the mantle of the earth.¹ Perovskite materials exhibit many interesting properties such as ferroelectricity, superconductivity, magnetoresistivity.²

The general chemical formula for perovskite compounds is ABX_3 , where 'A' and 'B' are two cations of different sizes, and 'X' is an anion that bonds to both. The 'A' and 'B' cations can have a variety of charges and in the original perovskite mineral (CaTiO_3) the 'A' cation is divalent and the 'B' cation is tetravalent. In the idealized cubic unit cell of perovskite structure (Figure 1.1), 'A' atom locates at cube corner positions (0, 0, 0), 'B' atom locates at body-centered position (1/2, 1/2, 1/2), and 'X' atoms locate at face-centered positions (1/2, 1/2, 0).

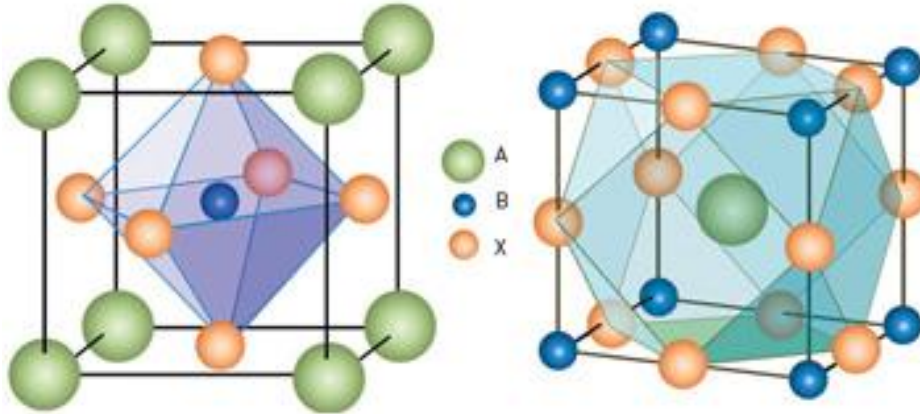


Figure 1.1. Crystal structure of perovskites (ABX_3).

Crystallographic behavior of perovskites is of great interest because most structures are close to an ideal cubic structure, however, frequently they are slightly distorted resulting in structures with lower symmetry such as orthorhombic, tetragonal, rhombohedral, trigonal systems and so on (Figure 1.2). These lattice distortions and structure changes are governed by temperature, pressure, chemical composition, and in some cases, electric field.³ The distorted structure may exist at room temperature, but it transforms to the ideal cubic structure at high temperature. This transition may occur in several steps through intermediate distorted phases. These deviations from the cubic perovskite structure may proceed from a simple distortion of the cubic unit cell, or an enlargement of the cubic unit cell, or a combination of both.

planes would be cut into halves. After the substitution by the appropriate organic molecules/ions, the monolayer inorganic perovskite slabs are sandwiched by the organic amine molecules and the corresponding 2D perovskites are produced, which can be expressed through $(R-NH_3)_2MX_4$ where $R-NH_3^+$ is an aliphatic or aromatic ammonium cation, 'X' is a halogen and 'M' is a divalent metal ions such as Cu^{2+} , Ni^{2+} , Co^{2+} , Fe^{2+} , Mn^{2+} , Pd^{2+} , Cd^{2+} , Ge^{2+} , Sn^{2+} , Pb^{2+} , *etc.* The basic structures of two-dimensional organic-inorganic perovskites are illustrated on Figure 1.3.

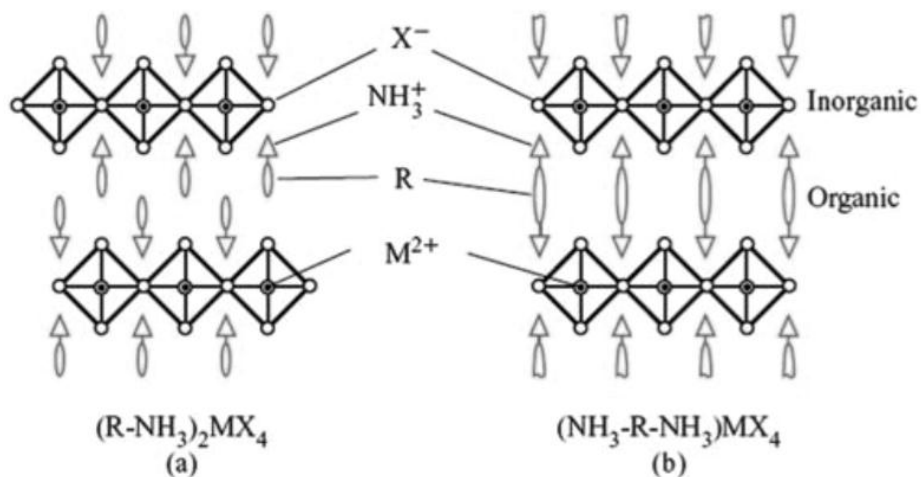


Figure 1.3. Schematic representation of the basic structures of two-dimensional organic-inorganic perovskites with (a) bilayer and (b) single layer intercalated organic molecules. (Ref. 2)

Since Miyasaka *et al.* first used the organic-inorganic hybrid perovskites in dye-sensitized solar cells (DSSCs),⁵ numerous researches on perovskite solar cells have been performed. Among the organic-inorganic hybrid perovskites studied so far, the most common is the methylammonium lead trihalide ($\text{CH}_3\text{NH}_3\text{PbX}_3$, $\text{X} = \text{Cl}^-, \text{Br}^-, \text{I}^-$) because of its superior intrinsic properties such as extremely long exciton diffusion length, high absorption coefficient, and excellent charge carrier transport.⁶⁻¹²

1.1.2 Advantages of organic-inorganic hybrid perovskites as solar cell material

Solar energy is one of clean, renewable energy sources that can solve the problems with worldwide energy crisis and global warming. Although the power conversion efficiencies (PCEs) of commercially available solar cells made of silicon, gallium arsenide, copper indium gallium selenide and cadmium telluride exceed 20%,¹³⁻¹⁸ the energy production costs of such solar cells are very high as compared to the energy cost produced by fossil fuels, which motivates us to develop low-cost solar cells. Organic-inorganic hybrid perovskite solar cells have recently attracted tremendous attention since its first report in 2009 because of its superior intrinsic properties such as extremely long diffusion length of charge carriers, excellent charge carrier transport, and high absorption coefficient.^{6-12, 19-23} Furthermore, thin films of organometal halide perovskite can be easily fabricated from abundant and inexpensive precursor materials. In spite of their short history, the photovoltaic performances of perovskite solar cells have advanced

dramatically with surpassing a PCE of 20%.²⁴ Hence, organic-inorganic hybrid perovskites have been recognized the most promising candidate for low-cost photovoltaics.

1.1.2.1 Charge carrier diffusion lengths

Organic photovoltaics (OPVs) have suffered from low efficiencies due to poor exciton or electron-hole diffusion lengths (typically about 10 nm). Because of the short charge carrier diffusion length, the structure of active layer for OPVs is limited. Bulk heterojunction structure has researched to solve this problem, but it is still difficult to optimize the processing condition for developing BHJ structure.

Xing *et al.* reported balanced long-range charge carrier diffusion lengths of over 100 nanometers in solution processed perovskite ($\text{CH}_3\text{NH}_3\text{PbI}_3$) by femtosecond transient optical spectroscopy with selective charge extraction (Figure 1.4).²⁵ Stranks *et al.* reported that the electron and hole diffusion length of mixed halide perovskite ($\text{CH}_3\text{NH}_3\text{PbI}_{3-x}\text{Cl}_x$) are larger than 1 micrometer, which is an order of magnitude higher than the absorption depth.⁶ Recently, Dong *et al.* reported that charge carrier diffusion lengths of $\text{CH}_3\text{NH}_3\text{PbI}_3$ single crystal are over 175 micrometers under 1 Sun, and exceed 3 millimeters under weak light.¹⁹ These extremely long charge carrier diffusion lengths result from high charge carrier mobility, long lifetime, and small trap density. Because the organic-inorganic hybrid perovskites have long charge carrier diffusion lengths, as reported so far, perovskite solar cells

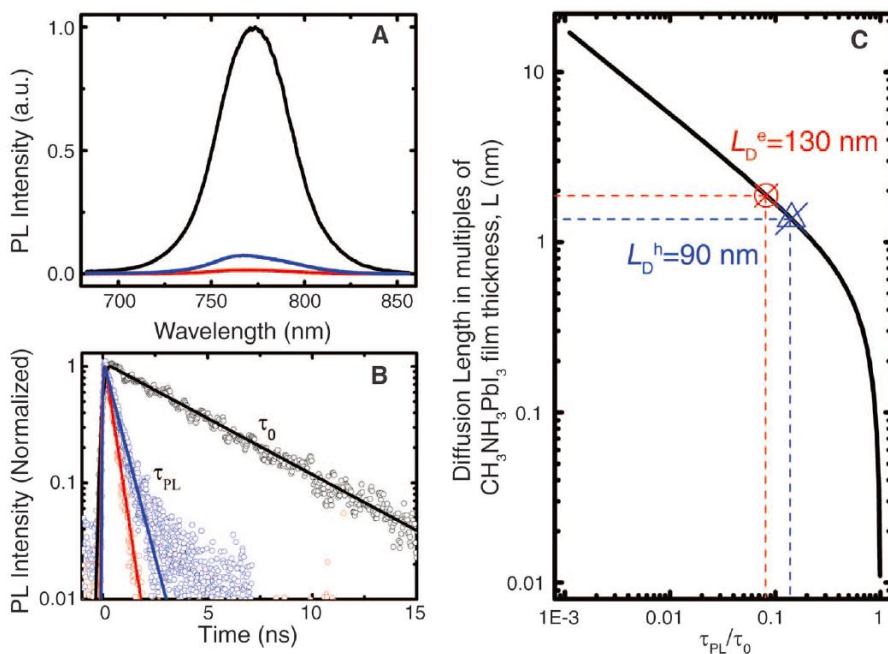


Figure 1.4. (A) Time-integrated photoluminescence (PL) spectra and (B) Time-resolved PL decay transients measured at 760 ± 10 nm for quartz/ $\text{CH}_3\text{NH}_3\text{PbI}_3$ (65 nm) (black), quartz/ $\text{CH}_3\text{NH}_3\text{PbI}_3$ (65 nm)/PCBM (red), quartz/ $\text{CH}_3\text{NH}_3\text{PbI}_3$ (65 nm)/spiro-OMeTAD (blue) films in vacuum after excitation at 600 nm. The solid lines in (B) are the single-exponential fits of the PL decay transients. (C) A plot of exciton diffusion length versus PL lifetime quenching ratios. Diffusion length is scaled in multiples of $\text{CH}_3\text{NH}_3\text{PbI}_3$ layer thickness ($L = 65$ nm). (Ref. 25)

afford high efficiency even with simple bilayer structure.

1.1.2.2 Charge carrier mobility

Charge carrier mobility of material plays an important role in charge transport in the matrix and charge collection at each electrode. Low charge carrier mobility results in slow charge extraction which causes charge recombination and deteriorates solar cell efficiency. In OPVs, space charge limited current (SCLC) mobilities of active layer materials are commonly ranged from 10^{-5} to 10^{-3} $\text{cm}^2 \text{V}^{-1} \text{s}^{-1}$, while the charge carrier mobilities of organic-inorganic perovskites are larger than $10 \text{ cm}^2 \text{V}^{-1} \text{s}^{-1}$. Dong *et. al.* measured charge carrier mobilities of $\text{CH}_3\text{NH}_3\text{PbI}_3$ single crystal (Figure 1.5).¹⁹ They reported that the hole-only device exhibits SCLC hole mobility of $165 \pm 25 \text{ cm}^2 \text{V}^{-1} \text{s}^{-1}$, while the electron-only device exhibits time-of-flight electron mobility of $24.0 \pm 6.8 \text{ cm}^2 \text{V}^{-1} \text{s}^{-1}$. These high charge carrier mobilities of organic-inorganic hybrid perovskite afford high efficiency of solar cell device and various applications.

1.1.2.3 Exciton binding energy

When a photon which has larger energy than bandgap of active layer material is penetrated to the solar cell device, an electron is excited from valence band to conduction band, generate a hole in valence band. This

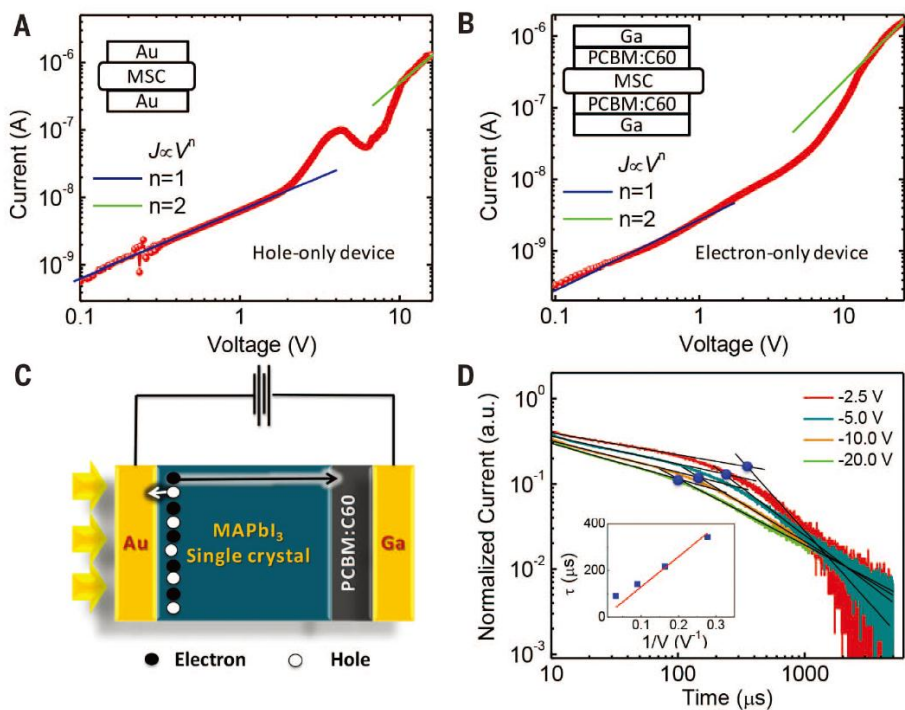


Figure. 1.5. Carrier mobility characterization of CH₃NH₃PbI₃ single crystal. Current-voltage curve for (A) a hole-only device and (B) an electron-only device. The insets show the device structure of hole-only and electron-only devices, respectively. (C) Schematic illustration of the device for the time-of-flight measurement. (D) The transient current curves of the CH₃NH₃PbI₃ single crystal device show the normalized transient photocurrent under various reverse biases. (Ref. 19)

electron-hole pair is called ‘exciton’ and is bound by Coulombic force. The exciton generated in active layer is dissociated into free electron and free hole when the built-in potentials at the active layer/charge transport layer interfaces are larger than the exciton binding energy. In OPVs, the exciton binding energy is about 0.3 eV, so the energy level offset between donor and acceptor materials should be larger than this value.

In organic-inorganic hybrid perovskite solar cells, however, the exciton binding energy is much lower than that of OPVs. Several groups reported that organic-inorganic perovskite ($\text{CH}_3\text{NH}_3\text{PbI}_3$) has quite low exciton binding energy less than 0.05 eV.^{21, 26-29} Therefore, the exciton generated in perovskite layer can be easily dissociated with relatively low energy level offset, and this afford wide choice of charge transporting layer materials.

1.1.2.4 Optical properties

Strong optical absorption is one of the key reasons for outstanding performance of organic-inorganic perovskite solar cells, reducing the required thickness of perovskite active layer.⁹ Organic-inorganic perovskites have large absorption coefficient of $>10^5 \text{ cm}^{-1}$ in visible range, as shown in Figure 1.6. Park *et al.* reported that $\text{CH}_3\text{NH}_3\text{PbI}_3$ quantum dot has one order of magnitude higher absorption coefficient than N719 dye, which is favorable material for DSSCs.⁸ Ziang *et al.* reported that $\text{CH}_3\text{NH}_3\text{PbI}_3$ exhibits three absorption peaks at 350 nm, 492 nm, and 776 nm.²⁰ Absorption peaks at 492 nm and 776 nm are attributed to transition from lower valence band minimum to the

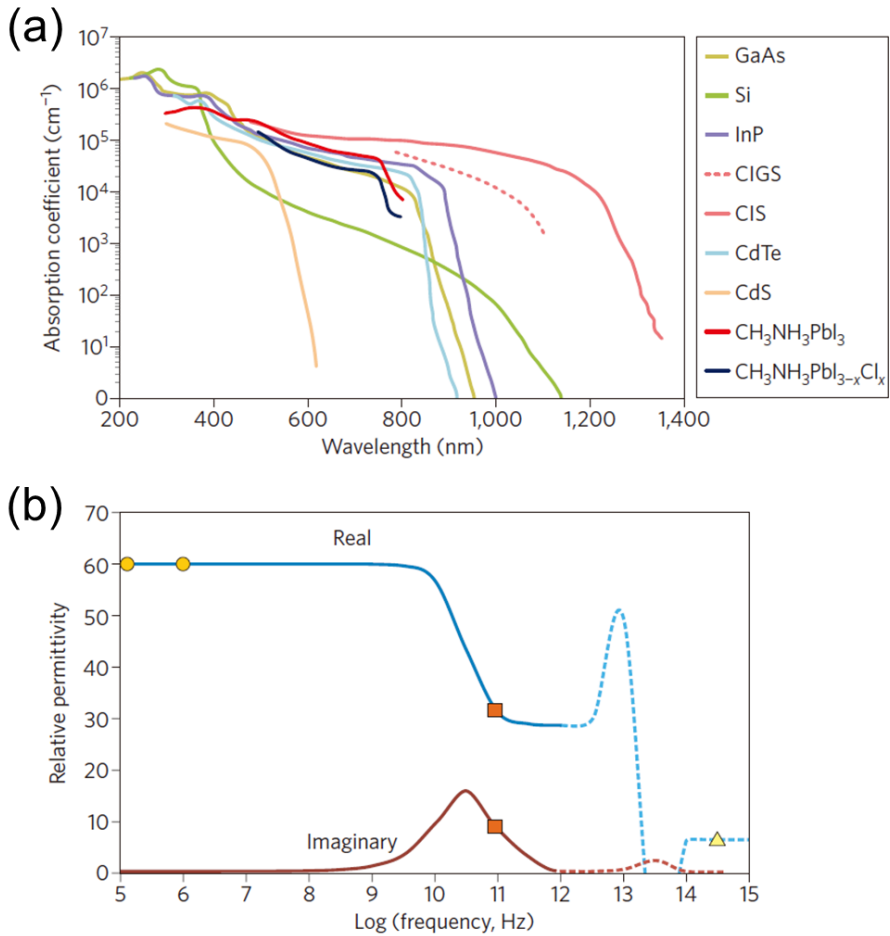


Figure. 1.6. (a) Absorption coefficient of $\text{CH}_3\text{NH}_3\text{PbI}_3$ and $\text{CH}_3\text{NH}_3\text{PbI}_{3-x}\text{Cl}_x$ compared to other solar cell materials. (b) Real and imaginary parts of the $\text{CH}_3\text{NH}_3\text{PbI}_3$ dielectric constant at 300 K as a function of frequency. (Ref. 9)

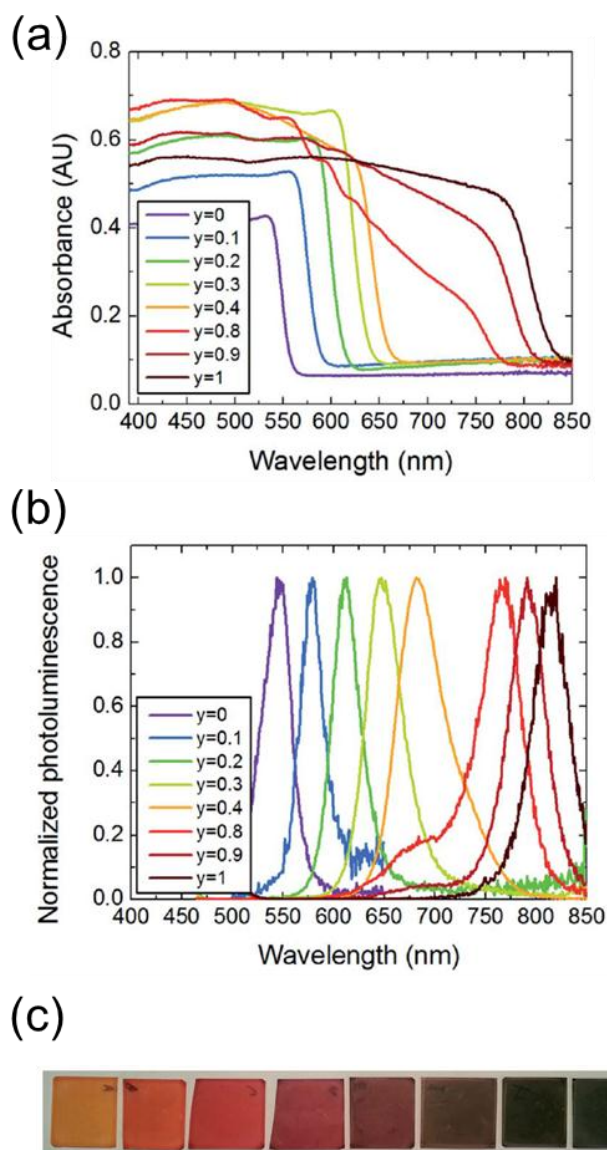


Figure. 1.7. (a) UV-Vis absorbance of the $\text{FAPbI}_y\text{Br}_{3-y}$ perovskites with varying y . (b) Corresponding steady-state photoluminescence spectra for the same films. (c) Photographs of the $\text{FAPbI}_y\text{Br}_{3-y}$ perovskite films with y increasing from 0 to 1 (left to right). (Ref. 12)

conduction band minimum, and direct gap transition of the $\text{CH}_3\text{NH}_3\text{PbI}_3$ from the first valence band maximum to the conduction band minimum, respectively, while the absorption peak at 350 nm is not assigned yet.

In addition to strong absorption property, organic-inorganic perovskites have easily tunable optoelectronic properties. Snaith *et al.* reported that as the A cation, in ABX_3 perovskite structure, increases in ionic radius, the lattice expand, the bandgap decreases, results in a red-shift of absorption spectrum.¹² Further, an increase in iodide fraction of mixed halide perovskite red-shifts the bandgap, as shown in Figure 1.7.

1.1.3 Classification by device structure

When Miyasaka *et al.* first developed the organic-inorganic perovskite solar cell, the device has DSSC structure of anode/mesoporous TiO_2 /perovskite sensitizer/cathode.⁵ Using 2,2',7,7'-tetrakis-(N,N-di-4-methoxyphenylamino)-9,9'-spirobifluorene (spiro-OMeTAD) as a solid-state hole transporting material, instead of using the liquid electrolyte, long-term stability of device has notably increased.³⁰ The most common device structure of this mesoscopic type perovskite solar cells is the configuration of FTO/compact TiO_2 /mesoporous TiO_2 /perovskite/spiro-OMeTAD/Au, as shown in Figure 1.8. For an alternative material to mesoporous TiO_2 , Al_2O_3 is successfully introduced and the device with Al_2O_3 exhibits excellent efficiency.³⁰⁻³¹ It is interesting to find that excited electrons are not injected into Al_2O_3 , which indicates that Al_2O_3 acts just as a scaffold layer and

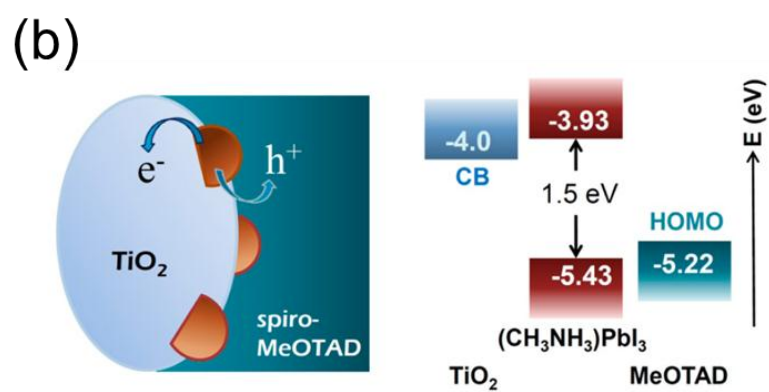
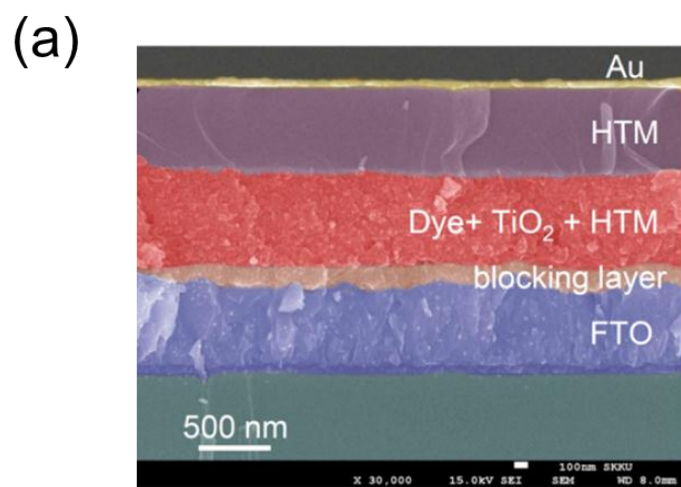


Figure 1.8. (a) Cross-sectional scanning electron microscope image of solid-state DSSC structure. (b) Schematic illustration of charge transfer in mesoscopic type perovskite solar cells and the energy levels of TiO₂, CH₃NH₃PbI₃, and spiro-OMeTAD.

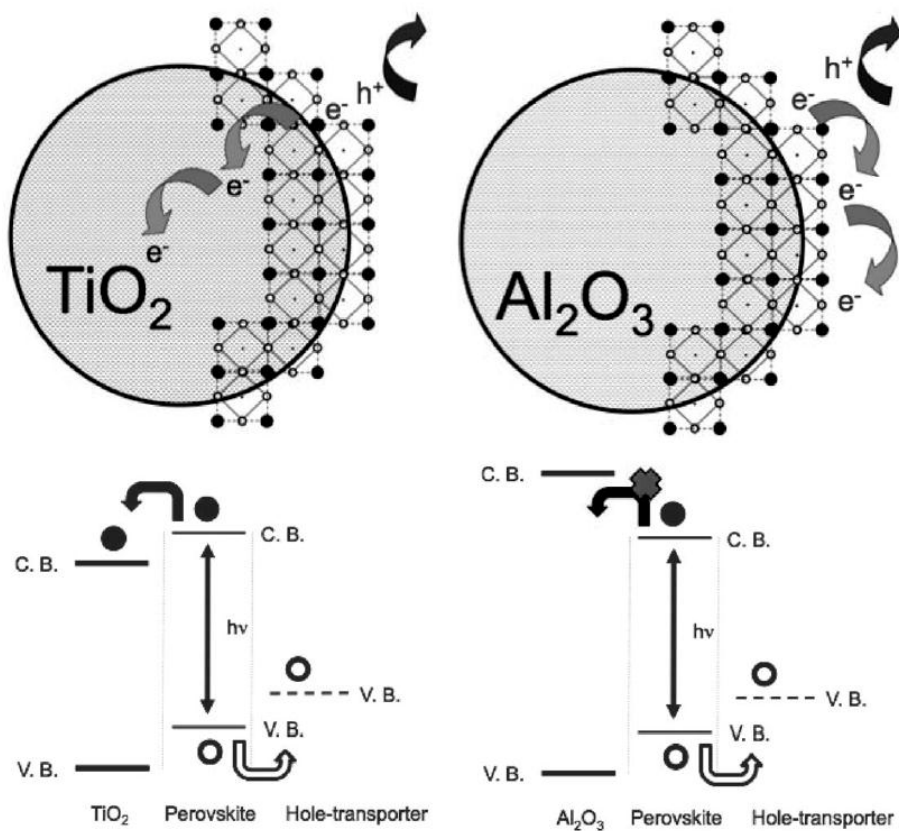


Figure 1.9. Schematic representation of the charge transfer and charge transport in a perovskite-sensitized TiO₂ solar cell and a non-injecting Al₂O₃-based solar cell. (Ref. 31)

perovskite layer acts as electron transporting layer (ETL) (Figure 1.9).

Rather than the mesoscopic type, planar heterojunction structure is simple and easy to fabricate the solar cell devices. Planar heterojunction perovskite solar cells are practical options for cost-effective and flexible solar cells owing to their low-temperature processibility contrary to the mesoscopic type. Planar heterojunction perovskite solar cells can be classified into two categories according to the stacking sequence of layers. The conventional n-i-p structure has a configuration of bottom cathode/ETL/perovskite/hole transporting layer (HTL)/top anode, while the inverted p-i-n structure has the inverse of the n-i-p structure.

1.1.4 Fabrication methods for organic-inorganic hybrid perovskite films

Fabricating perovskite film with high quality plays an important role in enhancing the performance of perovskite solar cells. Most widely used method is one-step deposition method due to its cost-effective, simple and easy process. For the one-step deposition method, $\text{CH}_3\text{NH}_3\text{I}$ and PbI_2 are prepared as organic and inorganic precursor, respectively. Two precursor materials are dissolved in an solvent such as N,N-dimethylformamide (DMF), dimethyl sulfoxide (DMSO), or γ -butyrolactone (GBL) and this is used as a spin-coating solution for fabricating $\text{CH}_3\text{NH}_3\text{PbI}_3$ films. Immediately after the spin-coating, the substrate needs to be annealed. The detail of the one-step deposition method is presented in section 2.1.3. Since the perovskite films

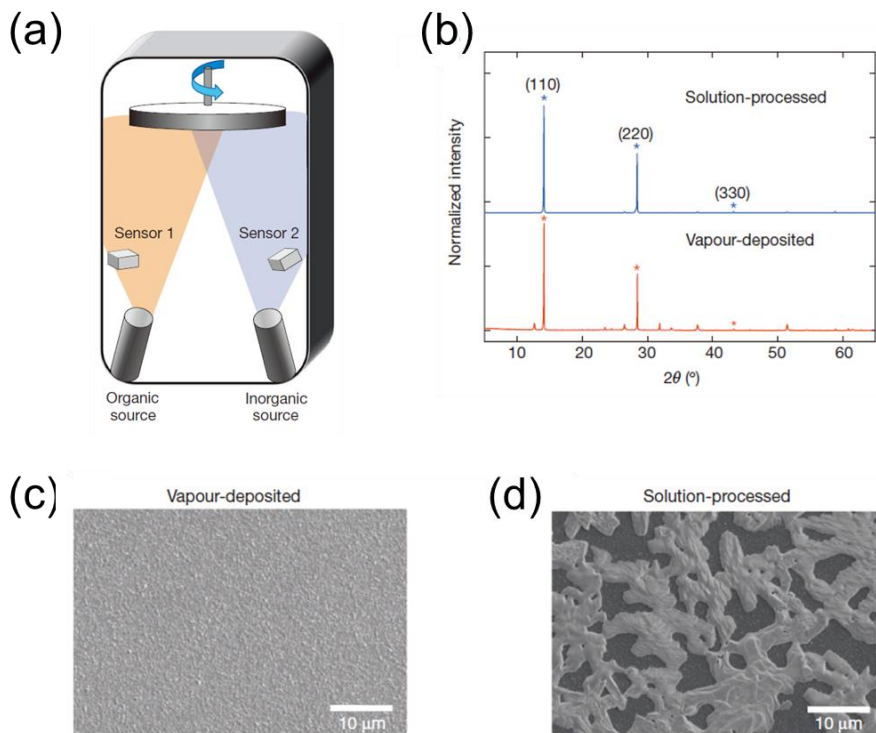


Figure 1.10. (a) Schematic representation of the dual-source thermal evaporation system for depositing the perovskite absorbers; the organic source is methylammonium iodide and the inorganic source is PbCl_2 . (b) X-ray diffraction spectra of a solution-processed perovskite film (blue) and vapour-deposited perovskite film (red). (c) SEM top view of a vapor-deposited perovskite film. (d) SEM top view of a solution-processed perovskite film. (Ref. 32)

fabricated by the one-step deposition method suffer from poor surface coverage with many pinholes, many researches include vapor deposition, two-step deposition, and solvent engineering have been conducted so far to improve the surface uniformity (Figure 1.10 and 1.11).³²⁻³⁵

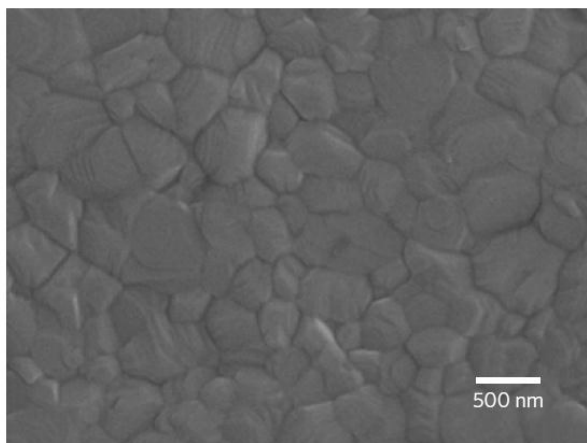
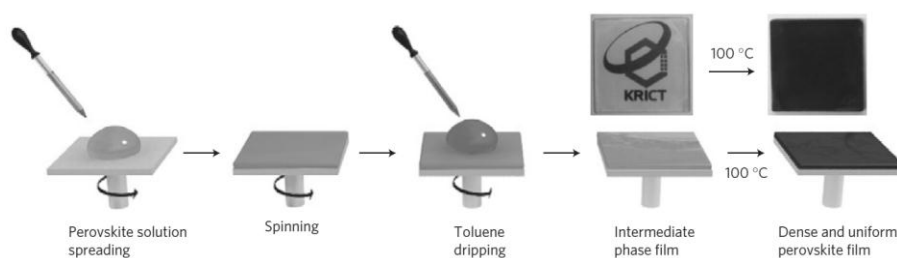


Figure 1.11. Schematic representation of solvent engineering procedure and SEM image of perovskite film fabricated by solvent engineering process. (Ref. 33)

1.2 Planar heterojunction perovskite solar cells with inverted device configuration

1.2.1 Operating principles

The solar cell is a device that converts light to electricity. The energy conversion process has multiple steps in the commonly accepted mechanism (Figure 1.12). Step 1 is light absorption. When the light is penetrated into the active layer of solar cell devices, the active layer material which has an appropriate bandgap absorbs the incident light. Because the methylammonium lead triiodide perovskite ($\text{CH}_3\text{NH}_3\text{PbI}_3$) has a bandgap of around 1.5 eV, organic-inorganic hybrid perovskite solar cells with $\text{CH}_3\text{NH}_3\text{PbI}_3$ active layer can absorb the light of ~800 nm wavelength range. Step 2 is formation of exciton and diffusion. Photon which has larger energy than the bandgap of active layer material excites an electron from valence band to conduction band, generate a hole in valence band. This electron-hole pair is called 'exciton' and is bound by Coulombic force. Step 3 is dissociation of the exciton. The exciton generated in active layer is dissociated into free electron and free hole due to the built-in potential at the active layer/charge transport layer interfaces. Step 4 is charge transport and collection. Transferred free charges are transported to each electrode and collected, then pass through the electric circuit to generate photocurrent. Electrons are transported by ETL and collected by cathode, while holes are transported by HTL and collected by anode. The charge carrier mobility of charge transporting layer plays a very important role in determining the solar cell efficiency.

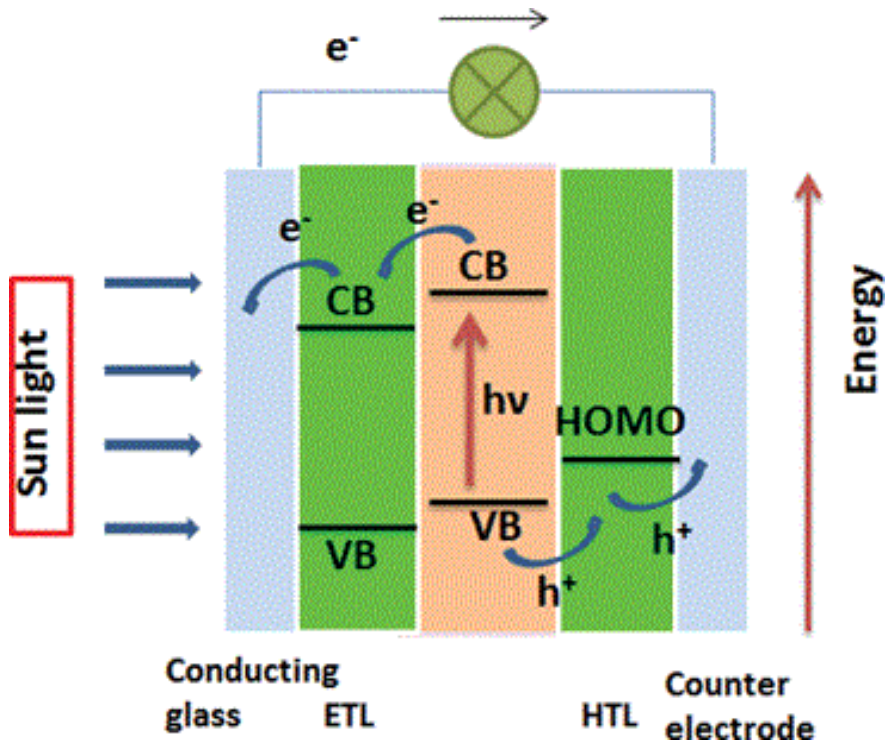


Figure 1.12. Fundamental operating principles of solar cells. (Ref. 36)

The current density–voltage curve of solar cell under illumination is illustrated in Figure 1.13. Voltage and current density are represented by X- and Y-axis, respectively. The power conversion efficiency of a solar cell is determined by the following formula:

$$FF = \frac{J_{\max} \times V_{\max}}{J_{sc} \times V_{oc}} \quad (1.1)$$

$$PCE = \frac{V_{oc} \times J_{sc} \times FF}{P_{in}} \quad (1.2)$$

where V_{OC} is the open circuit voltage defined by the point that the curve intersect with X-axis, J_{SC} is the short circuit current density defined by the point that the curve intersect with Y-axis, FF is the fill factor, and P_{in} is the incident light power density. This light intensity is standardized at 100 mW/cm^2 with a spectral intensity distribution matching the AM 1.5G

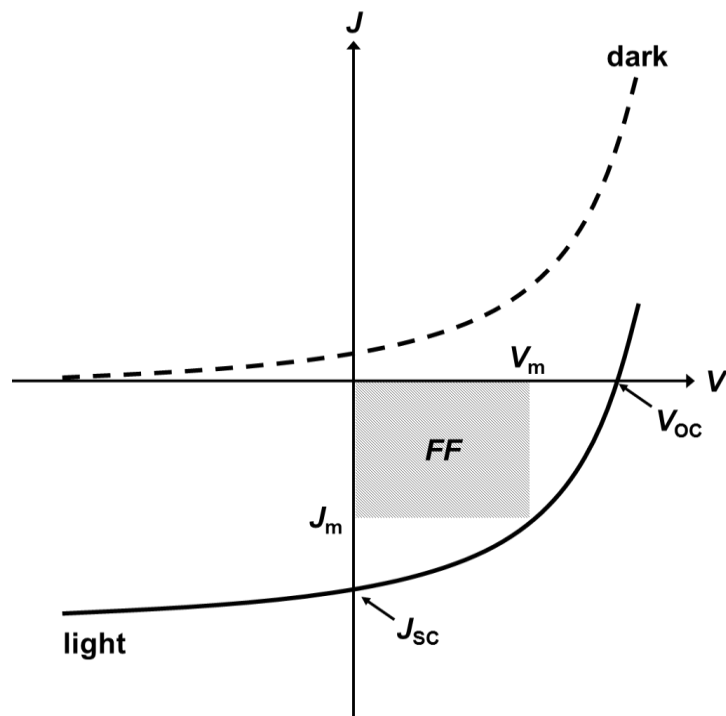


Figure 1.13. Current density–voltage curves of solar cells under illumination and in the dark. The photovoltaic parameters are represented.

condition. J_m and V_m are the current density and voltage at the maximum power point.³⁷

1.2.2 Device structure

Planar heterojunction perovskite solar cells can be classified into two types according to the device architecture: One is the normal structure with the n-i-p configuration of transparent electrode/compact TiO₂/perovskite/HTL/metal electrode, and another is the inverted structure with the p-i-n configuration of transparent electrode/HTL/perovskite/ETL/metal electrode which is similar to the OPV device structure (Figure 1.14). The most remarkable advantage of inverted structure over normal structure for perovskite solar cells is its simple and low-cost fabrication, because inverted perovskite solar cells can be fabricated by low-temperature solution process while normal perovskite solar cells require high temperature (>450 °C) sintering process to form compact TiO₂ layer. In addition, normal structure is difficult to be made flexible because most available flexible substrates (*e.g.*, PET, PEN) have a glass transition temperature (T_g) that is lower than the sintering temperature of compact TiO₂.³⁸ The devices with inverted structure, however, can be fabricated at low temperature (<150 °C), so this structure is adequate for flexible devices.

The first p-i-n type planar heterojunction perovskite solar cell was developed by Guo *et al.* in 2013.³⁹ They used PEDOT:PSS as a hole transporting material, and fullerene-based molecules as electron transporting

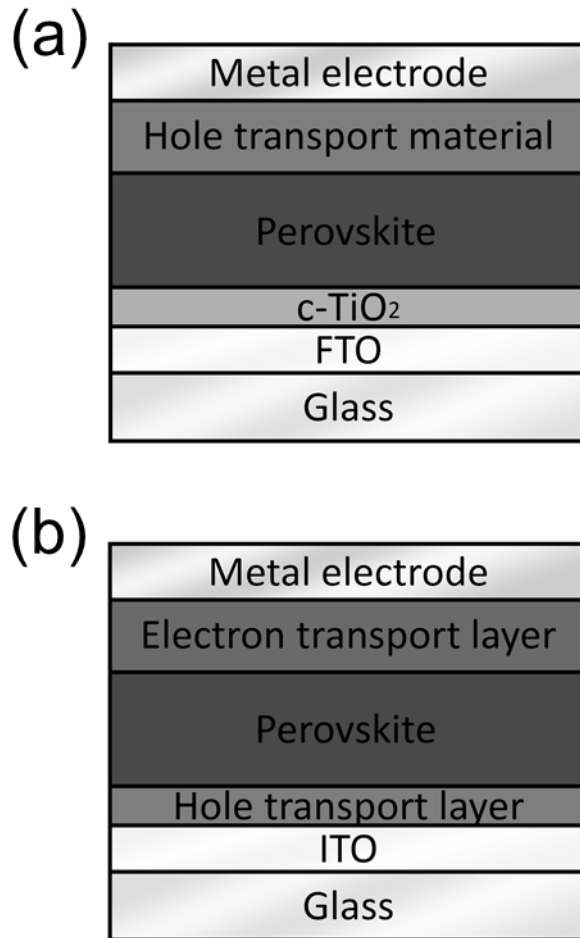


Figure 1.14. Schematic representation of device structure of planar heterojunction perovskite solar cells with (a) normal and (b) inverted configuration.

materials (Figure 1.15). In addition to PEDOT:PSS, various p-type materials such as NiOx, CuSCN, and graphene oxide have been reported as hole transporting material for efficient p-i-n type planar heterojunction perovskite solar cells.⁴⁰⁻⁴³ For ETL of planar heterojunction perovskite solar cells with inverted structure, fullerene derivatives such as C₆₀, phenyl-C₆₁-butyric acid

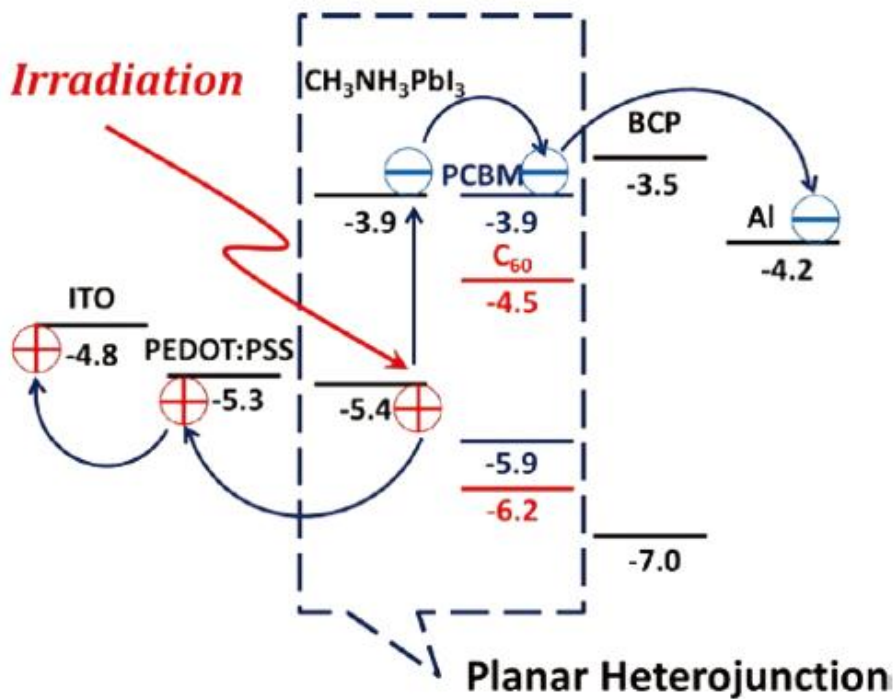


Figure 1.15. Energy levels of each layer of device with inverted planar heterojunction structure. (Ref. 39)

methyl ester (PCBM), bis-PCBM, and indene- C_{60} bisadduct (ICBA) have commonly been used because of their room temperature solubility and orthogonal solvent processibility on the perovskite layer (Figure 1.16).^{39, 44-46}

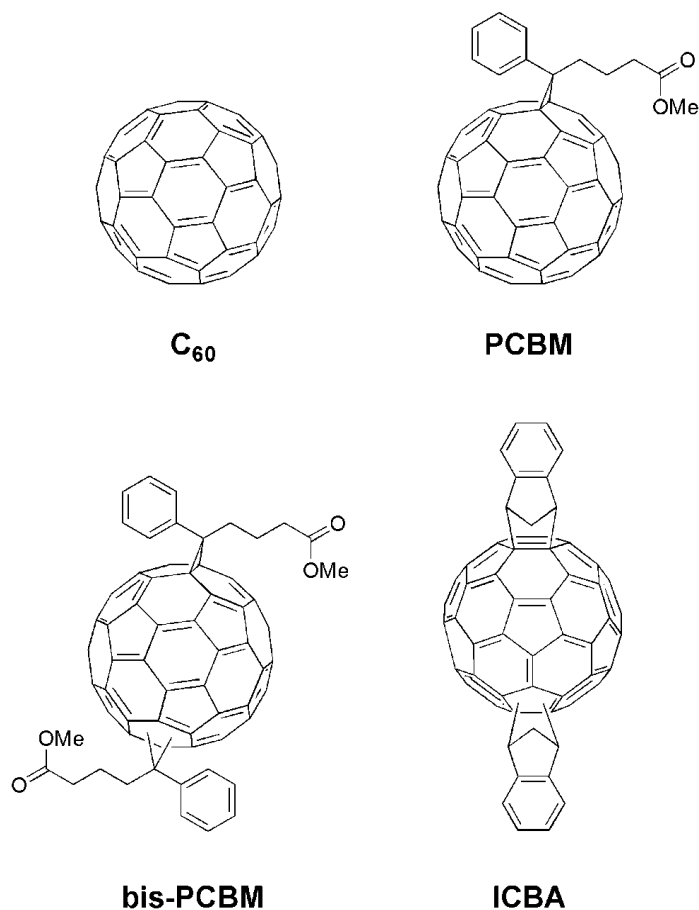


Figure 1.16. Chemical structures of *n*-type materials used as ETL materials for planar heterojunction perovskite solar cells with inverted device configuration.

1.2.3 *n*-Doping method

Thickness of ETL is very critical for achieving high performance of planar heterojunction perovskite solar cells with inverted structure, because sufficiently thick ETL is required to prevent direct contact between rough perovskite layer and metal cathode.⁴⁷ However, low electron mobility and low electrical conductivity of fullerene derivatives may limit the ETL thickness. When the thickness of PCBM was increased to 100 nm or thicker, the solar cell performance was notably diminished because of largely increased charge recombination.⁴⁸ Therefore, it is needed to increase the electrical conductivity of fullerene derivatives. One of effective ways to increase the electrical conductivity of fullerene is to dope or modify fullerenes, which may allow us to increase the ETL thickness and thus to achieve the performance enhancement of planar heterojunction perovskite solar cells.

1,3-Dimethyl-2-phenyl-2,3-dihydro-1*H*-benzimidazole (DMBI) derivatives have been reported as effective *n*-type dopants for enhancing the electrical properties of *n*-type materials such as fullerene or naphthalene diimide (NDI) derivatives.⁴⁹⁻⁵² Since DMBI has good solubility in common organic solvents, the doping is easily achieved by simply mixing with *n*-type material in organic solvents. Bao *et al.* reported that DMBI-doped PCBM films show a remarkably increased electrical conductivity (from 8.1×10^{-8} S/cm to 1.9×10^{-3} S/cm) and enhanced air stability (Figure 1.17).⁴⁹ They also reported that co-evaporated thin films of fullerene C₆₀ and *o*-MeO-DMBI-I exhibit a high electrical conductivity of 5.5 S/cm at a doping concentration of

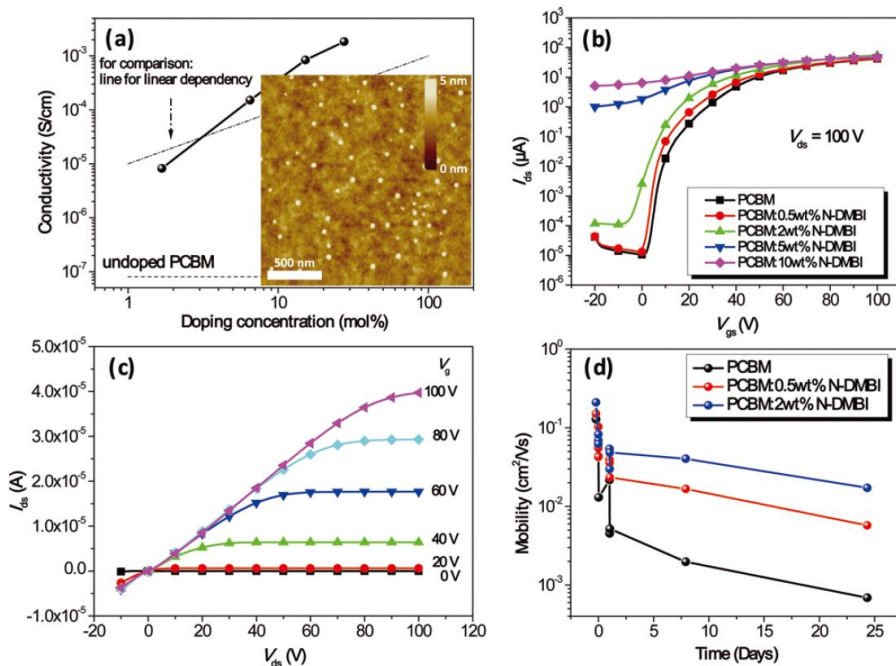


Figure 1.17. (a) Conductivities of undoped and N-DMBI-doped PCBM films at varying doping concentrations. Inset: AFM image of 2 wt% N-DMBI-doped PCBM film. (b) Transfer characteristics of N-DMBI-doped PCBM OTFTs at varying doping concentrations. (c) Output characteristics of 0.5 wt% N-DMBI-doped PCBM OTFTs. (d) Changes of field-effect mobilities in air as a function of time for undoped and 0.5 and 2 wt% N-DMBI-doped PCBM OTFTs. (Ref. 49)

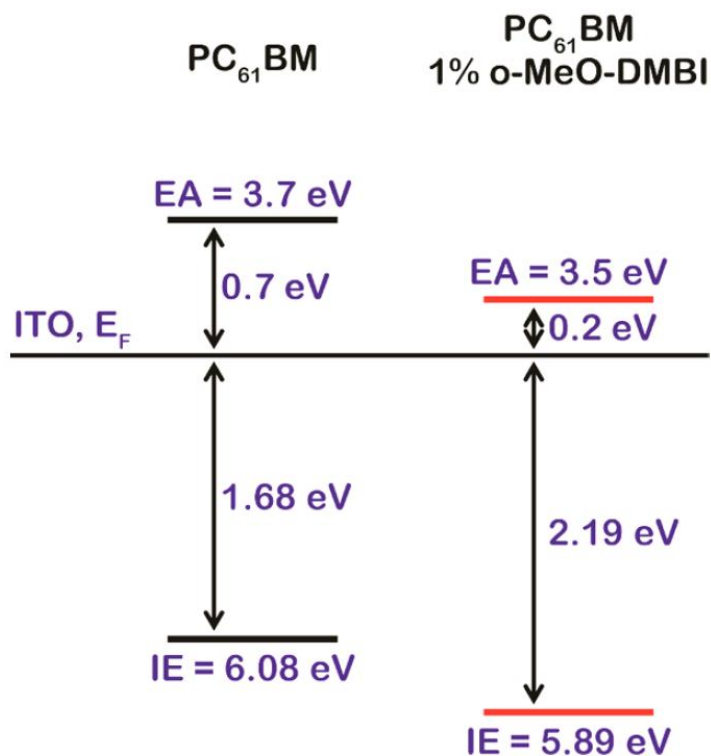


Figure 1.18. Energy level alignment of undoped and 1 wt% *o*-MeO-DMBI doped $PC_{61}BM$. (Ref. 51)

8 wt%.⁵⁰ It was also reported that the organic solar cell with DMBI-doped NDI-based ETL exhibited an enhanced PCE (from 0.69% to 3.42%).⁵²

Despite of the effectiveness of DMBI derivatives as *n*-type dopant, the doping of DMBI to fullerene derivatives in organic solar cells has not been studied yet. Since the planar heterojunction perovskite solar cells with

inverted structure commonly contain PCBM layer as ETL, DMBI is expected to effectively dope the PCBM and thus to enhance the solar cell performance of perovskite solar cells.

1.2.4 Non-fullerene electron acceptors

Design and synthesis of new hole transporting materials for normal perovskite solar cells have widely been studied by several groups in order to replace spiro-OMeTAD, because of relatively high production cost and low hole mobility of spiro-OMeTAD,⁵³⁻⁶¹ while new electron transporting materials of inverted cell as an alternative to PCBM have rarely been reported. So far, fullerene derivatives, especially PCBM is the most successful electron accepting materials for OPVs and planar heterojunction perovskite solar cells, due to its strong electron accepting ability, high electron mobility, isotropy of charge transport, and reversible electrochemical reduction.⁶² However, there still remains insufficiencies to overcome, such as weak absorption in visible range, limited absorption range, and limited tunability of energy levels by chemical modification.

In OPVs, non-fullerene electron acceptors based on polymers and small molecules have recently been developed because of their unique advantages over fullerene derivatives such as high absorption in visible range, tunable energy level, and low production cost.⁶³⁻⁷⁰ There have been a variety of non-fullerene acceptors include polymers and small molecules. Among those, rylene diimides have attracted great attention due to their adequate energy

levels, strong absorption, and high electron affinity. Many kinds of polymer acceptors have been designed so far, by incorporating rylene diimides such as perylene diimide (PDI), NDI, and their analogues. Since Zhan *et al.* first reported the study on PDI-based polymer which affords 1.03% of PCE in 2007,⁷¹ the efficiency of solar cells with PDI-based polymer has been greatly increased up to 7.7%.⁶⁶ Jenekhe *et al.* reported that NDI-based polymer

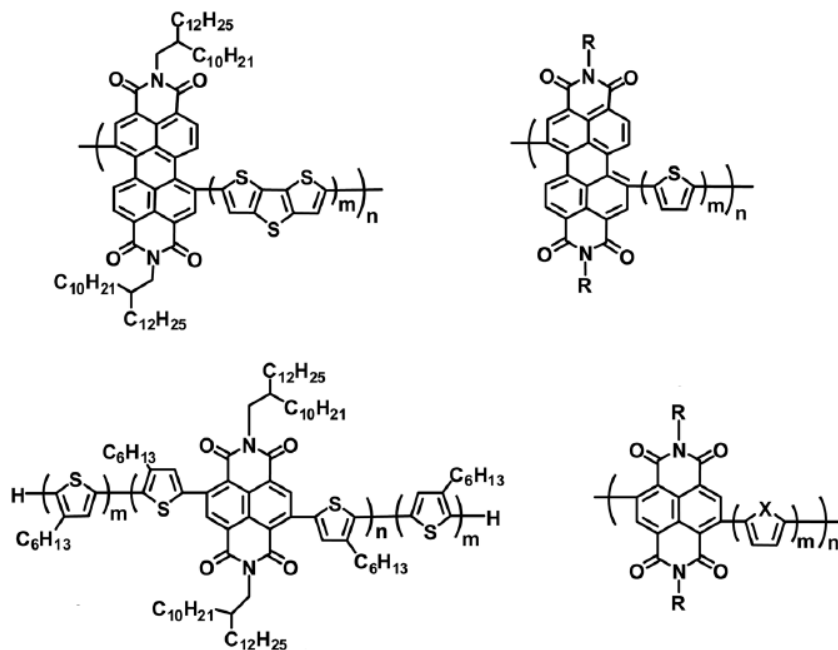


Figure 1.19. Chemical structures of PDI or NDI-based polymer acceptors.

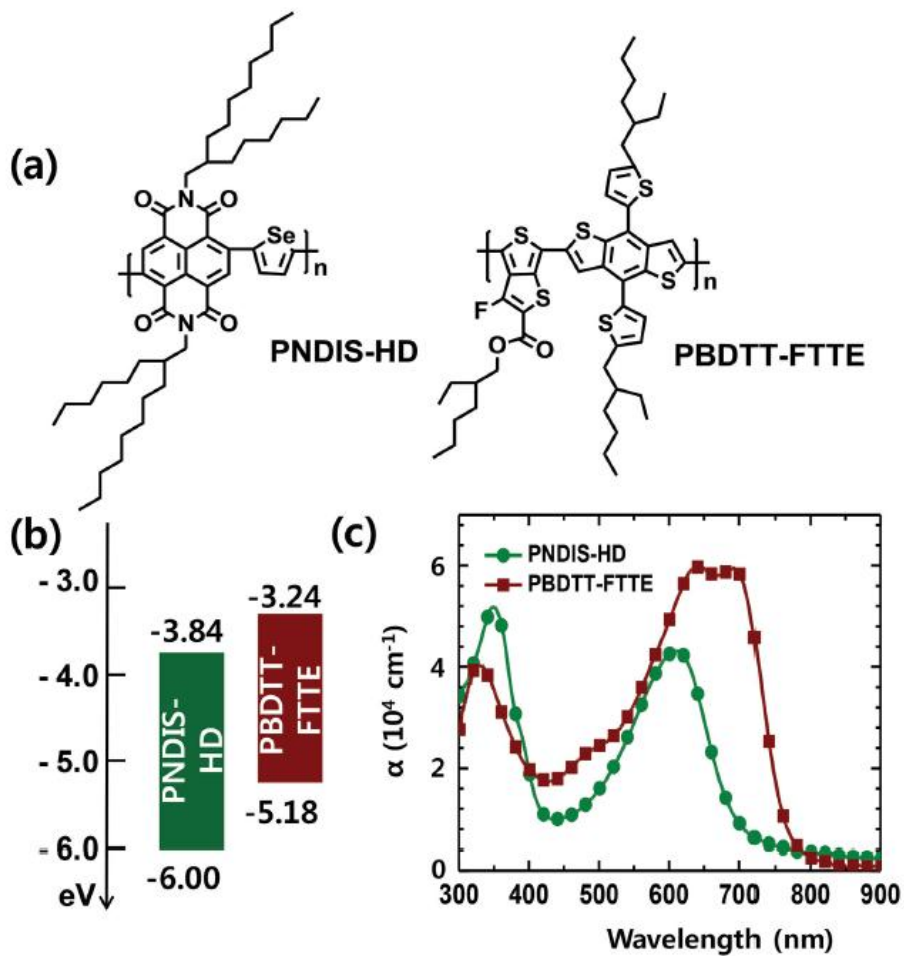


Figure 1.20. (a) Chemical structures of polymer acceptor (PNDIS-HD) and donor polymer (PBDTT-FTTE). (b) Energy levels of the acceptor and donor materials. (c) Optical absorption spectra of the acceptor and donor materials. (Ref. 66)

acceptor, PNDIS-HD, has a strong absorption and suitable energy level, results in remarkable efficiency of 7.7%.

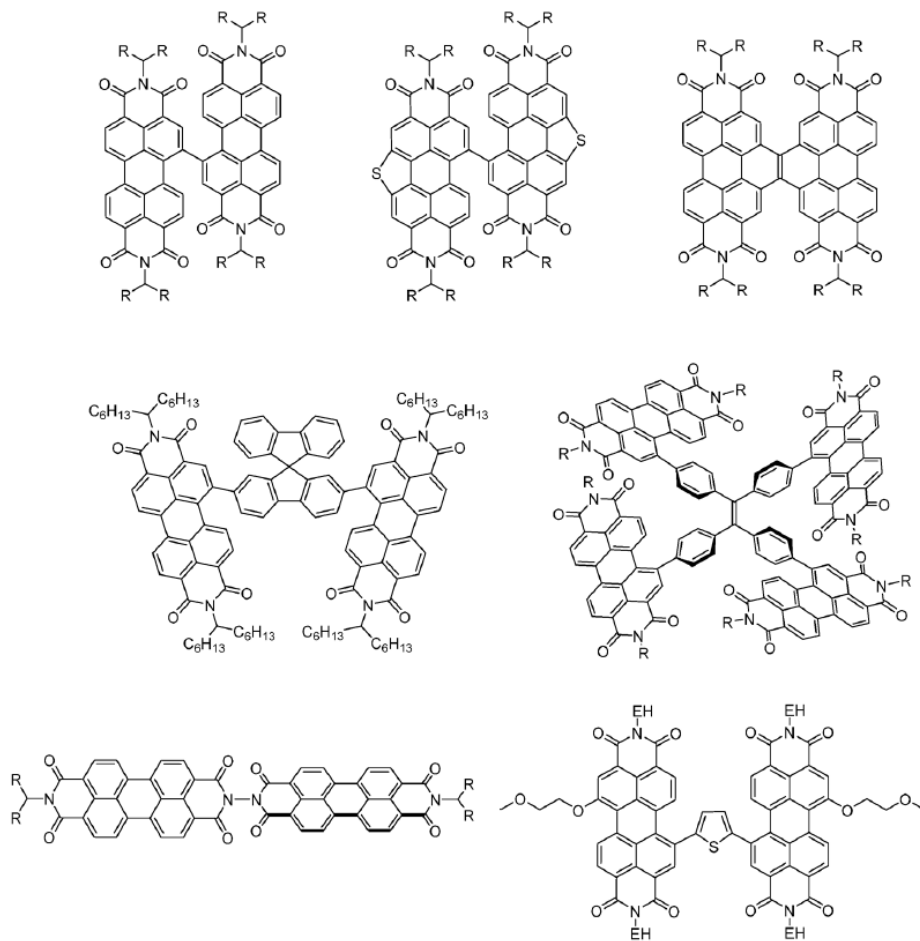


Figure 1.21. Chemical structures of PDI-based small molecule acceptors.

Meanwhile, small molecular rylene diimides also have been widely studied by several groups due to their advantages over polymer counterparts such as well-defined molecular structure and high purity.⁷² Wang *et al.* reported that solar cell device with PDI-based small molecule acceptor, SdiPBI-S, shows a high PCE of 7.16%.⁷³

Contrary to these tremendous attentions on non-fullerene acceptors in OPVs, introduction of non-fullerene acceptors to perovskite solar cells has rarely been studied. Since inverted perovskite solar cells require sufficiently thick ETL to prevent direct contact between perovskite layer and metal cathode,⁴⁷ the non-fullerene acceptors as electron transporting materials of perovskite solar cells should have sufficiently high electrical conductivity and high electron mobility.

1.3 Objectives of this study

Organic-inorganic hybrid perovskites have recently attracted enormous attention as the next generation material for photovoltaic devices due to their superior intrinsic properties such as long charge carrier diffusion length, excellent charge carrier transport, low exciton binding energy, high absorption coefficient, and easily tunable energy levels. Furthermore, thin films of organic-inorganic perovskites can be easily fabricated from abundant and inexpensive precursor materials.

Especially, planar heterojunction perovskite solar cell with an inverted device configuration of ITO/PEDOT:PSS/perovskite($\text{CH}_3\text{NH}_3\text{PbI}_3$)/electron

transporting material/Al has attracted much attention due to an advantage of low-temperature and solution processibility over the normal structure. While design and synthesis of new hole transporting materials for normal perovskite solar cells have widely been studied by several groups in order to replace spiro-OMeTAD because of its relatively high production cost and low hole mobility, new electron transporting material of inverted perovskite solar cells as an alternative to PCBM has rarely been reported.

In OPVs, non-fullerene electron acceptors based on polymers and small molecules have recently been developed because of their unique advantages over fullerene derivatives such as high absorption in visible range, tunable energy level, and low production cost. However, since inverted perovskite solar cells require sufficiently thick electron transporting layer to prevent direct contact between perovskite layer and metal cathode, the electron transporting material should have sufficiently high electrical conductivity and high electron mobility to effectively transport electrons to electrode without significant recombination. One of effective ways to increase the electrical conductivity is to dope materials, which may allow us to increase the ETL thickness and thus to achieve the performance enhancement of perovskite solar cells.

DMBI has been reported as an effective *n*-type dopant for enhancing the electrical properties of *n*-type materials such as fullerene or NDI derivatives. Since DMBI has good solubility in common organic solvents, the doping is easily achieved by simply mixing with *n*-type material in organic solvents. DMBI is expected to effectively dope the electron transporting materials and

thus to enhance the solar cell performance of planar heterojunction perovskite solar cells.

In this study, a simple *n*-doping method to enhance the electrical properties of *n*-type material is investigated in order to use the *n*-doped material as an ETL of planar heterojunction perovskite solar cells with inverted device configuration. *n*-Type materials used in this study are PCBM and diPDI which is perylene diimide (PDI)-based small molecule. First, we introduced an *n*-type dopant, DMBI, to dope the PCBM in perovskite solar cells with an inverted structure. DMBI is used to increase of electrical conductivity of PCBM, and results in the enhanced performance of solar cell devices with DMBI-doped PCBM ETL. Second, we used diPDI as a non-fullerene ETL material of inverted perovskite solar cells. Although the inherent electrical conductivity of diPDI is quite low, the successful introduction of diPDI to planar heterojunction perovskite solar cell becomes possible through the DMBI doping.

Chapter 2. Experimental Section

2.1 Synthesis and characterization

2.1.1 Materials

Methylamine (40% in methanol, TCI), hydriodic acid (57% w/w aqueous solution stabilized with 1.5% hypophosphorous acid, Alfa Aesar), anhydrous ethanol (>99.5%, Sigma-Aldrich), titanium(IV) chloride (>99.9%, Sigma-Aldrich), titanium diisopropoxide bis(acetylacetonate) (75 wt% in isopropanol, Sigma-Aldrich), benzyl alcohol (Extra dry, 98+%, Acros organics), *N,N'*-dimethyl-1,2-phenylenediamine (97%, Sigma-Aldrich), benzaldehyde (purified by re-distillation, >99.5%, Sigma-Aldrich), 3,4,9,10-perylenetetra-carboxylic dianhydride (98%, Alfa Aesar), 4-heptylamine (>98%, TCI), imidazole (>99.5%, Sigma-Aldrich), zinc acetate (99.99%, trace metals basis, Sigma-Aldrich), and copper powder (<100 nm particle size, 99.8%, Sigma-Aldrich) were purchased and used without further purification. Hydriodic acid was kept in refrigerator and anhydrous ethanol, titanium(IV) chloride, titanium diisopropoxide bis(acetylacetonate) and benzyl alcohol were kept in N₂-filled glovebox.

Methylammonium chloride (CH₃NH₃Cl) and methylammonium iodide (CH₃NH₃I) were used after drying at 60 °C in vacuum oven for more than 24 h. Lead iodide (99%) was purchase from Acros organics and dried in vacuum oven at 240 °C for 12 h. *N,N*-Dimethylformamide (anhydrous, 99.8%) and

dimethyl sulfoxide (anhydrous, >99.9%) were purchased from Sigma-Aldrich and 2-propanol (anhydrous, 99.5+%) was purchased from Alfa Aesar. Other organic solvents were used without further purification.

2.1.2 Synthesis of organic precursors of perovskite films

Methylammonium iodide: Methylammonium iodide ($\text{CH}_3\text{NH}_3\text{I}$) was synthesized by reacting equimolar methylamine with hydriodic acid. Hydriodic acid was added dropwise to methylamine solution at 0 °C with stirring. After 2 h, solvent was evaporated under reduced pressure by rotary evaporator. The product was recrystallized from ethanol and diethyl ether. After vacuum filtration, the precipitate was washed with diethyl ether several times and dried at 60 °C in vacuum oven for 24 h. ^1H NMR (300 MHz, DMSO- d_6): δ (ppm) 7.48 (s, 3H), 2.37 (s, 3H).

Methylammonium chloride: Synthesis of methylammonium chloride ($\text{CH}_3\text{NH}_3\text{Cl}$) was conducted similarly to $\text{CH}_3\text{NH}_3\text{I}$. Methylamine was reacted with equimolar amount of hydrochloric acid. Hydrochloric acid was added dropwise to methylamine solution at 0 °C with stirring. After 2 h, solvent was evaporated under reduced pressure by rotary evaporator. The product was recrystallized from ethanol and diethyl ether. After vacuum filtration, the precipitate was washed with diethyl ether several times and dried at 60 °C in vacuum oven for 24 h. ^1H NMR (300 MHz, DMSO- d_6): δ (ppm) 7.98 (s, 3H), 2.32 (s, 3H).

2.1.3 Fabrication of perovskite films

1.18 mmol of organic precursor material ($\text{CH}_3\text{NH}_3\text{I}$) and lead iodide were mixed and dissolved in 1 mL of anhydrous DMSO. The weighing procedure was conducted in N_2 -filled glovebox. The solution was stirred at $60\text{ }^\circ\text{C}$ for 3 h and cooled to room temperature. The solution was filtered by $0.2\text{ }\mu\text{m}$ polytetrafluoroethylene (PTFE) syringe filter before use. The final precursor solution was used for fabricating perovskite films within 2 days.

Spin-coating process and heat treatment were conducted in N_2 -filled glovebox. The final precursor solution was spin-coated at 3000 rpm for 15 s and the substrate was immediately transferred to a preheated hot plate. The substrate was annealed at $110\text{ }^\circ\text{C}$ for 30 s to form a perovskite ($\text{CH}_3\text{NH}_3\text{PbI}_3$) film.



Figure 2.1. Schematic representation of perovskite film fabrication method.

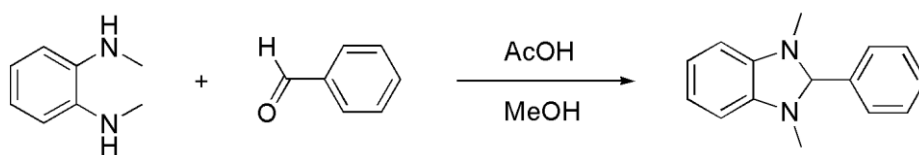
2.1.4 Synthesis of titanium dioxide nanoparticles

Titanium dioxide nanoparticles were synthesized to use as an electron extracting interlayer between electron transporting layer and metal cathode. Synthetic process was conducted in the N₂-filled glovebox. 0.5 mL of titanium(IV) chloride was added slowly to 2 mL of anhydrous ethanol with stirring then the whole content was mixed with 10 mL of anhydrous benzyl alcohol. The solution was heated at 80 °C. After 6 h, slightly translucent suspension was obtained. 3 mL of resulting suspension was precipitated in 27 mL of diethyl ether. To isolate TiO₂ nanoparticles, the precipitate was centrifuged at 5000 rpm and then redispersed in ethanol (6 mg/mL). 14.7 μL of titanium diisopropoxide bis(acetylacetonate) was added to 1 mL of redispersed TiO₂ nanoparticle solution.

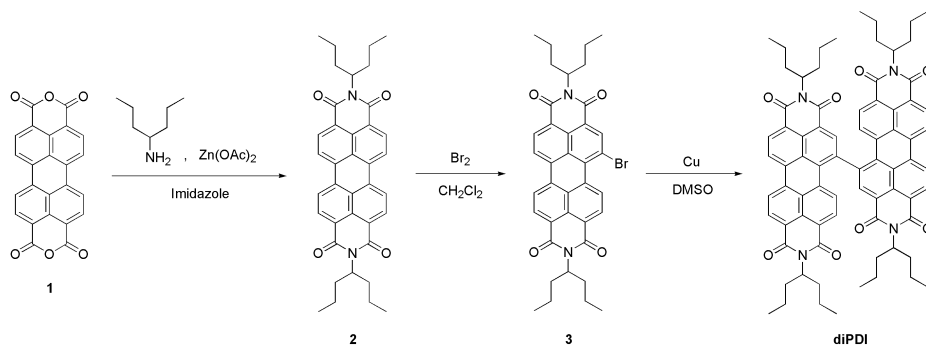
2.1.5 Synthesis of *n*-type dopant

n-Type dopant DMBI was synthesized to effectively dope the *n*-type materials used in this study. A 20 mL scintillation vial was charged with 136 mg (1.00 mmol) of *N,N'*-dimethyl-*o*-phenylenediamine and 0.1 mL (1.00 mmol) of benzaldehyde in 2 mL of methanol. Then one drop of glacial acetic acid was added, and the solution was sonicated at room temperature for 1 h. The mixture dissolved in methanol and evaporated under reduced pressure by rotary evaporator. The product was recrystallized from small amount of methanol. After vacuum filtration, the precipitate was washed with methanol and dried at 60 °C in vacuum oven for 48 h. ¹H NMR (300 MHz, DMSO-d₆):

δ (ppm) 7.50-7.57 (m, 2H), 7.41-7.49 (m, 3H), 6.59-6.64 (m, 2H), 6.41-6.48 (m, 2H), 4.87 (s, 1H), 2.48 (s, 6H).



Scheme 2.1. Synthetic scheme of DMBI.



Scheme 2.2. Synthetic scheme of diPDI.

2.1.6 Synthesis of non-fullerene acceptors

2.1.6.1 Synthesis of *N,N'*-bis(1-propylbutyl)perylene-3,4:9,10-tetracarboxylic diimide

A mixture of 1.00 g (2.55 mmol) of 3,4,9,10-perylenetetracarboxylic dianhydride (**1**), 0.72 g (6.25 mmol) of 4-heptylamine, 5.00 g (73.44 mmol) of imidazole, and 351 mg (1.91 mmol) of zinc acetate was stirred at 160 °C for 2 h. After being cooled to room temperature, the mixture dissolved in chloroform and purified by column chromatography on silica gel using chloroform as an eluent to afford a red solid of **2** (1286 mg, 86%). ¹H NMR (300 MHz, CDCl₃): δ (ppm) 8.68 (d, 4H), 8.63 (d, 4H), 5.24 (m, 2H), 2.28 (m, 4H), 1.83 (m, 4H), 1.34 (m, 8H), 0.93 (t, 12H).

2.1.6.2 Synthesis of 1-bromo-*N,N'*-bis(1-propylbutyl)perylene-3,4:9,10-tetracarboxylic diimide

A mixture of 1.00 g (1.70 mmol) of compound **2** and 13.72 g (0.086 mol) of bromine in 50 mL of dichloromethane was stirred at 25 °C for 4 days. The mixture poured into ice-water, and then stirred for 1 h with addition of sodium thiosulfate. Then the mixture was extracted with dichloromethane for 3 times. After the organic phase was dried over MgSO₄, the solvent was evaporated under reduced pressure by rotary evaporator. The crude product was purified by column chromatography on silica gel using chloroform as an eluent. The second band afforded an orange solid of 1-bromo-*N,N'*-bis(1-propylbutyl)perylene-3,4:9,10-tetracarboxylic diimide **3** (359 mg, 32%). ¹H

NMR (300 MHz, CDCl₃): δ (ppm) 9.8 (m, 1H), 8.93 (s, 1H), 8.6-8.75 (m, 5H), 5.23 (m, 2H), 2.26 (m, 4H), 1.82 (m, 4H), 1.32 (m, 8H), 0.93 (t, 12H).

2.1.6.3 Synthesis of diPDI

A mixture of 260 mg (0.39 mmol) of compound **3** and 248 mg (3.90 mmol) of copper powder in 40 mL of DMSO was stirred at 100 °C for 8 h. The cooled mixture was poured into water, and then extracted with chloroform. After the organic phase was dried over MgSO₄, the solvent was evaporated under reduced pressure by rotary evaporator. The crude product was purified by column chromatography on silica gel using dichloromethane and hexane mixture (3:1, v:v) as an eluent to afford a deep red solid of diPDI (82 mg, 36%). ¹H NMR (300 MHz, CDCl₃): δ (ppm) 8.79 (d, 8H), 8.48 (d, 2H), 8.17 (s, 4H), 5.16 (m, 4H), 2.20 (m, 8H), 1.75 (m, 8H), 1.28 (m, 16H), 0.88 (t, 24H).

2.1.7 Characterization methods

The chemical structures of compounds were identified by ¹H NMR (Avance DPX-300). XRD patterns were obtained by X-ray diffractometer (D8 Advance, Bruker) using Cu-K α ^{1,2} radiation ($\lambda = 1.5418 \text{ \AA}$) at a scan rate of 2 ° min⁻¹. The UV-Vis-NIR absorption spectra were obtained by UV-Vis spectrophotometer (Lambda 25, Perkin Elmer). The PL emission spectra were obtained by using a Shimadzu spectrofluorometer (RF-5301PC). Cyclic voltammetry measurements were conducted on a potentiostat/galvanostat

(VMP 3, Biologic) in an electrolyte solution of 0.1 M tetrabutylammonium hexafluorophosphate acetonitrile. Pt wires (Bioanalytical System Inc.) were used as both counter and working electrodes, and silver/silver ion (Ag in 0.1 M AgNO₃ solution, Bioanalytical System Inc.) was used as a reference electrode. The highest occupied molecular orbital (HOMO) energy levels of materials were calculated by using the following relation: HOMO (eV) = $-[E_{\text{ox}} - E_{1/2}(\text{ferrocene}) + 4.8]$, where E_{ox} is the onset oxidation potential of the polymer and $E_{1/2}(\text{ferrocene})$ is the onset oxidation potential of ferrocene vs. Ag/Ag⁺.

UPS measurement was performed using a hemispherical electron energy analyzer (RESOLVE 120, PSP). The base pressure of analysis chamber was maintained under low 10⁻⁹ Torr. He I ($h\nu = 21.22$ eV) discharge lamp was used as an excitation source with sample bias of -15 and -10 V for secondary electron cutoff and valence band region, respectively. Fermi level was calibrated through Ar⁺-sputtered clean Au. The electrical conductivities of DMBI-doped and un-doped films were measured for the devices with planar diode structure. The devices for measurement of electrical conductivity were fabricated by spin-coating of DMBI-doped or un-doped solution on the top of pre-cleaned (in the order of deionized water, acetone, and isopropanol, 30 mins each) glass followed by thermal deposition of Au in a vacuum below 10⁻⁷ Torr. Au parallel electrode bars with 80 nm thick were separated with a distance of 70 μm. The electrical conductivity was measured by a probe station with a computer-controlled Keithley 4200 source measurement unit. Devices for electrical conductivity measurement had a channel length of 50

μm and a channel width of 1 mm. Film thickness was measured by AFM measurement. PL lifetimes were measured by using 400 nm, second harmonic generated Ti:Sapphire femtosecond laser (MaiTai, Spectra Physics) as excitation source and time-correlated single photon counting module (MPD-PDM Series DET-40 photon counting detector and Pendulum CNT-91 frequency counter) combined with monochromator as detector. The parameter of PL decay were obtained by fitting the spectra with a biexponential decay function, $I(t) = A_1 \exp(-t/\tau_1) + A_2 \exp(-t/\tau_2)$. Average lifetime, τ_{ave} were calculated by equation, $\tau_{\text{ave}} = A_1\tau_1 + A_2\tau_2$.⁷⁴

2.2 Device fabrication and measurements

2.2.1 Materials

ITO coated glass ($10 \Omega \text{ sq}^{-1}$) was purchased from KETI. Poly(3,4-ethylenedioxy-thiophene):poly(styrenesulfonate) (PEDOT:PSS, Clevis P VP AI 4083) was purchased from Heraeus. [6,6]-Phenyl-C61-butyric acid methyl ester (PC₆₁BM, 99.5%) was purchased from nano-C. Chloroform (anhydrous, >99%) and chlorobenzene (anhydrous, 99.8%) were purchased from Sigma-Aldrich. Aluminum (99.999%) and gold (99.99%) were purchased from Taewon scientific. Calcium (99.5%) was purchased from Alfa Aesar. Acetone (99.7%) and 2-propanol (99.5%) were purchased from Samchun chemical. 10 mg of PC₆₁BM was dissolved in 1 mL of anhydrous chloroform. 6 mg/mL of TiO₂ nanoparticles dispersion in anhydrous ethanol with an additive of 14.7

μL of titanium diisopropoxide bis(acetylacetonate) was diluted 4 times for spin-coating on PC₆₁BM.

2.2.2 Fabrication of solar cell devices

2.2.2.1 Fabrication of solar cell devices with PCBM ETL

The configuration of the solar cell devices with PCBM ETL is glass/ITO/PEDOT:PSS/CH₃NH₃PbI₃/PCBM or PCBM:DMBI/Ca/Al. The ITO-coated glass was cleaned by stepwise sonication in acetone and isopropanol for 30 min each. After complete drying at 120 °C in convection oven, the ITO-coated glass was treated with UV-ozone for 15 min. A 40 nm thick PEDOT:PSS was spin-coated on the ITO-coated glass at 3000 rpm for 40 s. The substrate was annealed at 150 °C for 30 min in ambient condition. Then, substrates were transferred to N₂-filled glove box and annealed further at 120 °C for 10 min. For the perovskite (CH₃NH₃PbI₃) layer, a 1:1 ratio of CH₃NH₃I:PbI₂ was dissolved in DMSO with concentration of 1.18 M. The precursor solution was spin-coated onto the PEDOT:PSS layer at 3000 rpm for 15 s. The substrate was immediately transferred onto a hot plate and heated at 110 °C for 30 s. For the ETL, various ratios of PCBM/DMBI solutions were used. Same concentration (10 and 20 mg/mL in chloroform) of PCBM solution and DMBI solution were prepared and mixed with various ratios (0.5 wt% (398 μL of PCBM + 2 μL of DMBI), 1 wt% (198 μL of PCBM + 2 μL of DMBI), 3 wt% (194 μL of PCBM + 6 μL of DMBI), and 5 wt% (190 μL of PCBM + 10 μL of DMBI)). Then the mixed solutions were

spin-coated on $\text{CH}_3\text{NH}_3\text{PbI}_3$ layer at 3000 rpm for 30 s. 10 and 20 mg/mL chloroform solutions were used for fabrication of 50 and 105 nm thick ETL, respectively. The device was transferred to thermal evaporator, then 40 nm of Ca and 120 nm of aluminum were deposited under vacuum ($<10^{-6}$ Torr) through a shadow mask to give a device area of 0.1 cm^2 .

2.2.2.2 Fabrication of solar cell device with non-fullerene ETL

The configuration of the solar cell device with non-fullerene ETL is glass/ITO/PEDOT:PSS/ $\text{CH}_3\text{NH}_3\text{PbI}_3$ /diPDI or diPDI:DMBI/ TiO_2 /Al. The fabrication procedure from the cleaning of ITO to the spin-coating of perovskite layer was conducted identically to the case of PCBM ETL. For the ETL, various ratios of diPDI/DMBI solutions were used. Same concentration (20 mg/mL in chlorobenzene) of diPDI solution and DMBI solution were prepared and mixed with various ratios (0.5 wt% (398 μL of diPDI + 2 μL of DMBI), 1 wt% (198 μL of diPDI + 2 μL of DMBI), 3 wt% (194 μL of diPDI + 6 μL of DMBI), and 5 wt% (190 μL of diPDI + 10 μL of DMBI)). Then the mixed solutions were spin-coated on $\text{CH}_3\text{NH}_3\text{PbI}_3$ layer at 3000 rpm for 30 s. Then, TiO_2 nanoparticles dispersion was spin-coated on the ETL at 3000 rpm for 40 s. The device was transferred to thermal evaporator and 100 nm of aluminum was deposited under vacuum ($<10^{-6}$ Torr) through a shadow mask to give a device area of 0.1 cm^2 .

2.2.3 Solar cell performance measurements

J-V curves of photovoltaic cells were obtained using a computer-controlled Keithley 4200 source measurement unit under AM 1.5G (100 mW cm^{-2}) simulated by an Oriel solar simulator (Oriel 91160A). The light intensity was calibrated using a NREL-certified photodiode prior to each measurement. Range of bias sweep was from 2 V to -1 V. Data points were placed with an interval of 0.01 V and delay time was 0.01 s. The external quantum efficiency (EQE) was measured using Polaronix K3100 measurement system (Mcscience). EQE was measured with a range from 300 nm to 900 nm. Data points were placed with an interval of 20 nm and calculated average value of 5 times measurements. The light intensity at each wavelength was calibrated with a standard single-crystal Si cell.

Chapter 3. Results and Discussion

3.1 Performance enhancement of inverted structure planar heterojunction perovskite solar cells by *n*-doping of PCBM electron transporting layer

3.1.1 Synthesis and characterization

Organic-inorganic hybrid perovskites ($\text{CH}_3\text{NH}_3\text{PbX}_3$) are easily produced by fast reaction of organic precursor ($\text{CH}_3\text{NH}_3\text{X}$) and inorganic precursor (PbX_2). Organic precursor molecules penetrate into inorganic precursor framework and change the structure (e.g. from edge sharing of PbI_6 octahedron in PbI_2 to corner sharing of $\text{CH}_3\text{NH}_3\text{PbI}_3$). For fabrication of methylammonium lead triiodide ($\text{CH}_3\text{NH}_3\text{PbI}_3$), methylammonium iodide ($\text{CH}_3\text{NH}_3\text{I}$) as an organic precursor and lead(II) iodide (PbI_2) as a inorganic precursor are widely used and synthetic procedure of $\text{CH}_3\text{NH}_3\text{I}$ was report in many studies.⁷⁵⁻⁸¹ Fabrication of $\text{CH}_3\text{NH}_3\text{PbI}_3$ perovskite film is schematically represented in Figure 2.1. Synthesized $\text{CH}_3\text{NH}_3\text{I}$ through the method that was explained in experimental section was confirmed by ^1H NMR (Figure 3.1). Three protons each at methyl group and ammonium group are detected at 2.37 ppm and 7.48 ppm, respectively. Two peaks show same integration area due to the same number of protons at methyl group and ammonium group.

DMBI, an *n*-type dopant for ETL of inverted structured perovskite solar cells, was synthesized by reacting *N,N'*-dimethyl-*o*-phenylenediamine with

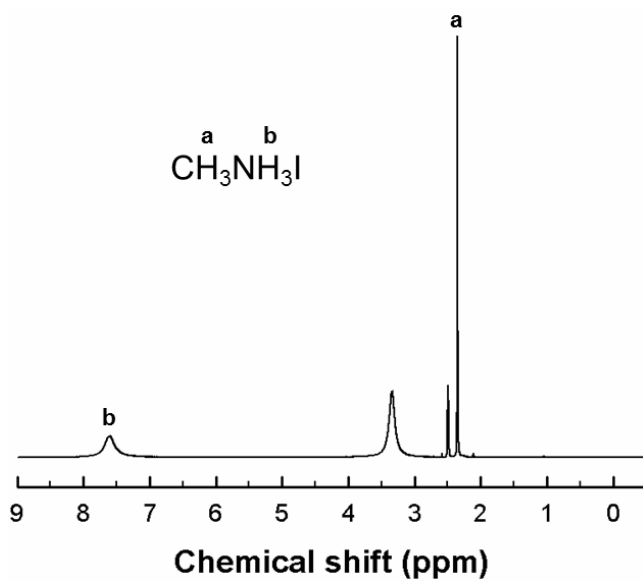


Figure 3.1. ^1H NMR spectrum of methylammonium iodide.

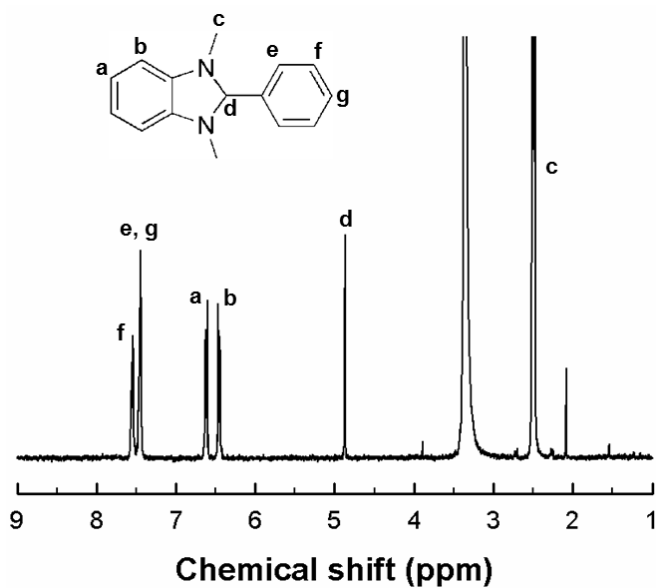


Figure 3.2. ^1H NMR spectrum of DMBI.

equimolar benzaldehyde as shown in Scheme 2.1. Synthesized DMBI through the method that was explained in experimental section was confirmed by ^1H NMR (Figure 3.2.). Synthesized DMBI has good solubility in common organic solvents such as chloroform and chlorobenzene, and therefore the *n*-doped PCBM layer is easily fabricated by spin-coating of a mixed solution of PCBM and DMBI in common solvent.

3.1.2 Characterization of *n*-doping

For inverted structured planar heterojunction perovskite solar cells, fullerene derivatives such as C_{60} , phenyl- C_{61} -butyric acid methyl ester (PCBM), PC_{71}BM , and indene- C_{60} bisadduct (ICBA) have widely been used as electron transporting layer material because of their room temperature solubility and orthogonal solvent processibility on the perovskite layer. Thickness of ETL is very critical for achieving high performance of inverted structure perovskite solar cells, because sufficiently thick ETL is required to prevent direct contact between rough perovskite layer and metal cathode.⁴⁷ However, low electron mobility and low electrical conductivity of fullerene derivatives may limit the ETL thickness. When the thickness of PCBM was increased to 100 nm or thicker, the solar cell performance was notably diminished because of largely increased charge recombination.⁴⁸ Therefore, it is needed to increase the electrical conductivity of fullerene derivatives. One of effective ways to increase the electrical conductivity of fullerene is to dope or modify fullerenes, which may allow us to increase the ETL thickness and

thus to achieve the performance enhancement of PHJ perovskite solar cells.

Electrical conductivities of pristine PCBM film and DMBI-doped PCBM film were measured to investigate the effect of *n*-doping on electrical conductivity. The electrical conductivity of DMBI-doped PCBM film is 6.1×10^{-5} S/cm which is 4 orders of magnitude higher than that of pristine PCBM film (3.8×10^{-9} S/cm), as measured for the device with planar diode structure by a probe station (see section 2.1.7), indicating that the doping by DMBI increases largely the electrical conductivity of PCBM.

When UV–Vis–NIR absorption spectra of pure PCBM and DMBI-doped PCBM were measured and compared, as shown in Figure 3.3, the DMBI-doped PCBM films exhibit a broad peak centered at 900 nm, while the peak intensity increases with the doping concentration, indicating that PCBM radical anions are formed in DMBI-doped PCBM.⁸² Therefore, it is concluded that DMBI effectively dopes the PCBM in the simple mixture by donating an electron to PCBM.

Ultraviolet photoelectron spectroscopy (UPS) spectra were measured to examine the change of the Fermi level and the HOMO energy level with doping (Figure 3.4). The work functions of films are determined by subtracting the binding energy cutoffs in high binding energy region (Figure 3.4a) from the He I photon energy (21.22 eV), while the binding energy cutoffs in low binding energy region (Figure 3.4b) indicate the energy gap between the Fermi levels and the HOMO energy level. The work function of PCBM is decreased from 5.04 eV to 4.76 eV upon addition of DMBI, as can be seen in Figure 3.5b. In other words, an addition of DMBI shifts the Fermi

level of PCBM toward the lowest unoccupied molecular orbital (LUMO) energy level, which is another evidence of *n*-doping. Therefore, the up-shift of the Fermi level due to *n*-doping of PCBM leads us to expect enhancement of electron transporting property of PCBM and thereby an increase in photocurrent of the solar cell device with *n*-doped PCBM ETL.

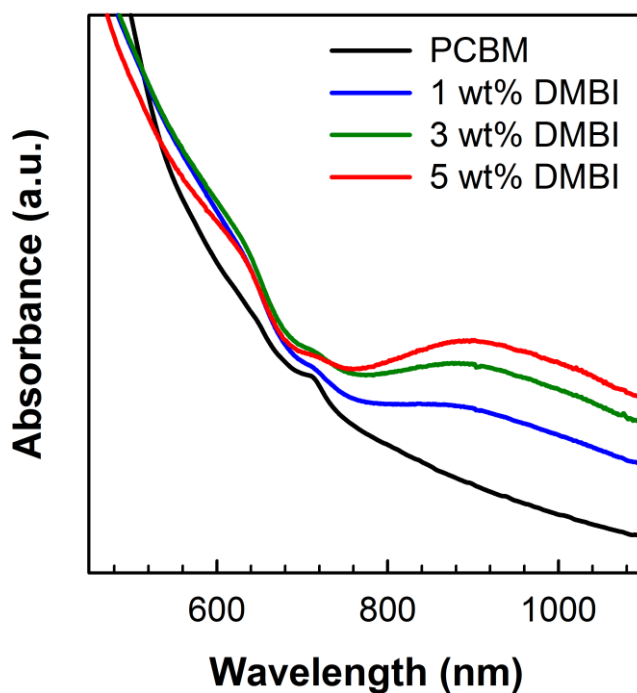


Figure 3.3. UV-Vis-NIR absorption spectra of pure PCBM film and DMBI-doped PCBM films with various doping concentrations. All films are fabricated by spin-coating the chloroform solution on glass.

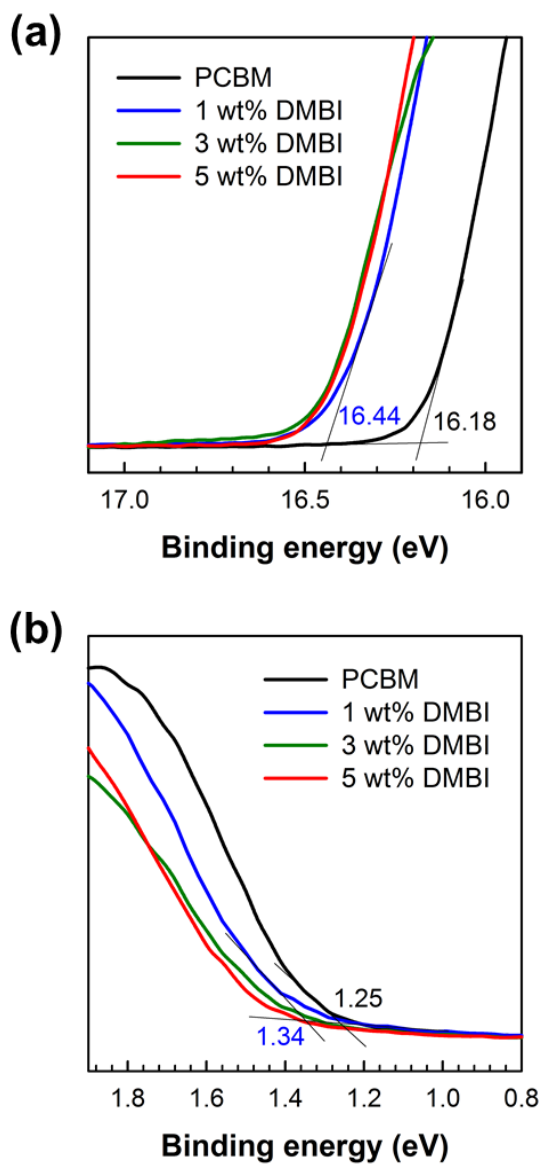


Figure 3.4. UPS spectra of pure PCBM and DMBI-doped PCBM with various doping concentrations for (a) high binding energy region and (b) low binding energy region. Binding energy cutoffs of PCBM and PCBM doped with 1 wt% DMBI are indicated.

3.1.3 Photovoltaic properties

When the current density–voltage curves of perovskite solar cells are measured with an inverted device configuration of ITO/PEDOT:PSS/CH₃NH₃PbI₃/PCBM or PCBM:DMBI/Ca/Al (Figure 3.5a), J_{SC} is notably enhanced by the addition of DMBI to the 50 nm-thick PCBM ETL, as shown in Figure 3.6 and Table 3.1. The PCE is increased from 12.3% with a J_{SC} of 19.1 mA cm⁻² to 13.0% with a J_{SC} of 21.0 mA cm⁻², when 1 wt% DMBI is added. Particularly, the increase of J_{SC} upon addition of 1 wt% DMBI is attributed to an increased number of free electrons due to the up-shift of the Fermi level. Increased electrical conductivity of DMBI-doped PCBM film is clear evidence of this argument. When the addition of DMBI is further increased, both J_{SC} and V_{OC} remain nearly unchanged while FF is decreased, indicating that the optimum addition of DMBI is 1 wt%. The reason for the decrease of FF will be discussed later.

Fabrication of a thick PCBM layer has an advantage of easy processing in industry while the increase of the PCBM layer thickness decreases the PCE probably due to increased recombination and high series resistance, which arise mainly from the low electrical conductivity of PCBM.⁸³ Hence, an increase of the electrical conductivity of PCBM is essential for the fabrication of a thick PCBM layer without compromising the device performance. Therefore, the dramatically increased electrical conductivity of PCBM by n-doping may lead to high PCE in the devices with a thick PCBM layer. When one compares the doping effect on the photovoltaic performance for thin

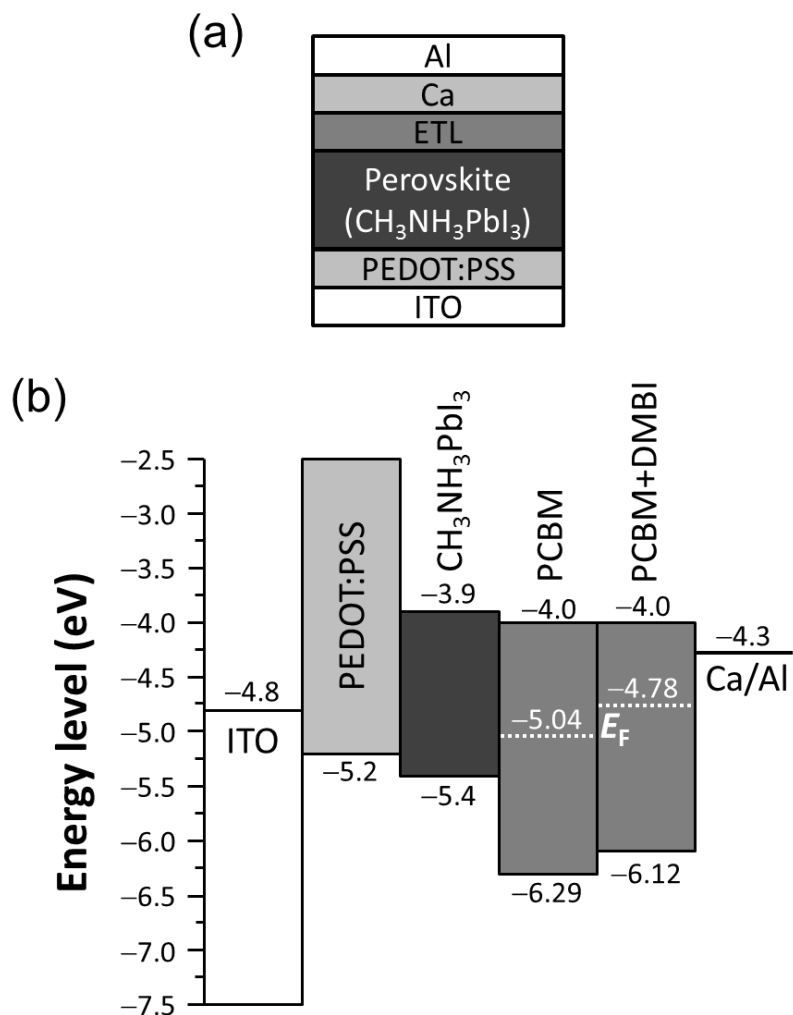


Figure 3.5. (a) Schematic of the device architecture used in this work. (b) Energy levels of each layer. Fermi levels (E_F) and HOMO energy levels of the ETL were determined for pure PCBM and 1 wt% doped PCBM by UPS measurements.

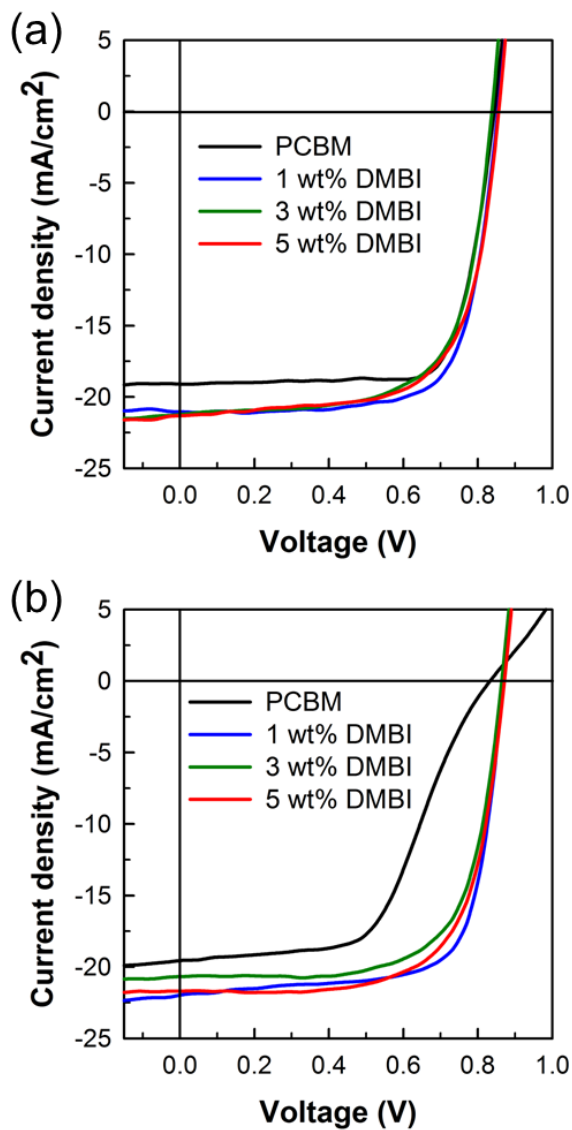


Figure 3.6. J - V curves of the devices with (a) a thin (50 nm) ETL which are fabricated by spin-coating of 10 mg mL^{-1} chloroform solution, and (b) a thick (105 nm) ETL which are fabricated by spin-coating of 20 mg mL^{-1} chloroform solution.

Table 3.1. The best photovoltaic properties of devices with PCBM ETL with different thickness and different dopant concentrations.

Solution conc.^a (mg/mL)	Dopant conc. of ETL	J_{sc} (mA cm⁻²)	V_{oc} (V)	FF	PCE (%)	R_{sh}^b (Ω cm²)	R_s^b (Ω cm²)
10	Pure PCBM	19.1	0.84	0.77	12.3	1.42×10^3	3.52
10	1 wt% DMBI	21.0	0.85	0.73	13.0	9.97×10^2	3.60
10	3 wt% DMBI	21.2	0.84	0.68	12.1	5.88×10^2	3.62
10	5 wt% DMBI	21.3	0.86	0.67	12.3	4.01×10^2	3.85
20	Pure PCBM	19.6	0.83	0.55	8.9	4.11×10^2	35.1
20	1 wt% DMBI	22.0	0.87	0.72	13.8	5.04×10^2	3.71
20	3 wt% DMBI	20.7	0.86	0.70	12.4	5.35×10^2	3.96
20	5 wt% DMBI	21.7	0.87	0.69	13.0	5.17×10^2	4.24

^a10 and 20 mg/mL chloroform solutions are used for fabrication of 50 and 105 nm thick ETL, respectively.

^bThe series and shunt resistance were calculated by the slopes of J - V curves.

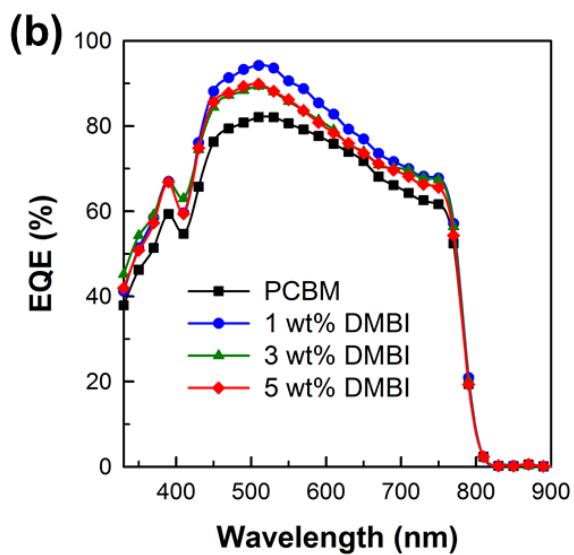
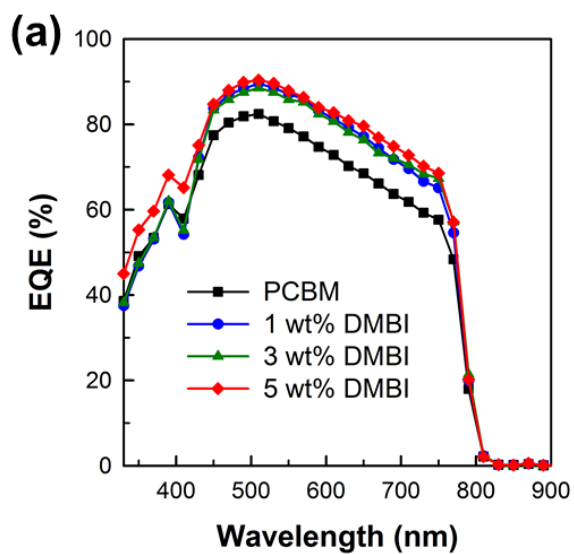


Figure 3.7. EQE spectra of devices with (a) thin ETL and (b) thick ETL which are doped with various DMBI concentrations.

Table 3.2. Average device parameters and their standard deviations based on at least 10 devices.

Solution conc.^a (mg/mL)	Dopant conc. of ETL	J_{sc}^b (mA cm⁻²)	V_{oc} (V)	FF	PCE (%)
10	Pure PCBM	18.2±1.1 (18.2)	0.82±0.05	0.72±0.05	11.0±1.0
10	1 wt% DMBI	20.3±0.8 (20.0)	0.84±0.02	0.70±0.05	12.1±0.8
10	3 wt% DMBI	20.3±1.3 (20.0)	0.83±0.03	0.67±0.04	11.1±1.0
10	5 wt% DMBI	20.5±1.2 (20.6)	0.83±0.03	0.65±0.05	11.1±0.9
20	Pure PCBM	18.4±0.9 (18.6)	0.82±0.04	0.52±0.07	7.9±1.2
20	1 wt% DMBI	20.6±0.8 (20.6)	0.86±0.02	0.69±0.05	12.2±0.7
20	3 wt% DMBI	20.0±0.7 (19.9)	0.84±0.03	0.69±0.03	11.2±0.7
20	5 wt% DMBI	19.9±1.0 (19.8)	0.84±0.05	0.67±0.04	11.6±1.0

^a10 and 20 mg/mL chloroform solutions are used for fabrication of 50 and 105 nm thick ETL, respectively.

^b J_{sc} values calculated from EQE spectra are indicated in parenthesis.

PCBM (Figure 3.6a) with that for a thick PCBM layer (Figure 3.6b), it is revealed that the doping effect by DMBI is more remarkable than for the thick PCBM layer. As shown in Figure 3.6b, the device with a 105 nm-thick PCBM layer exhibits an S-shaped J - V curve with a low FF of 0.55, while the device with 1 wt% DMBI-doped PCBM shows a remarkably improved FF of 0.72, probably due to reduced series resistance (Table 3.1), and as a result the PCE is increased from 8.9% ($J_{SC} = 19.6 \text{ mA cm}^{-2}$ and $V_{OC} = 0.83 \text{ V}$) to 13.8% ($J_{SC} = 22.0 \text{ mA cm}^{-2}$ and $V_{OC} = 0.87 \text{ V}$) upon addition of 1 wt% DMBI. The J_{SC} values calculated from the external quantum efficiency spectra also show that J_{SC} increases when PCBM is doped by DMBI (Figure 3.7 and Table 3.2), which are very consistent with the J_{SC} s measured from the J - V curves within 5% error. Since it has been well recognized that the charge accumulation is the key factor for the S-shaped curve,⁸⁴ the above result leads us to conclude that the doping by DMBI increases the electrical conductivity of PCBM and therefore prevents charge accumulation by generating free electrons in the PCBM layer. In short, the addition of a small amount of DMBI (1 wt%) allows us to fabricate the devices with a thick PCBM layer without loss in the solar cell performance.

3.1.4 Effects of excessive doping on photovoltaic properties

When the addition of DMBI is increased more than 1 wt%, the FF of the device is slightly decreased for both cases of thin and thick ETLs, as shown in Table 3.1. The atomic force microscopy images of the film surfaces have

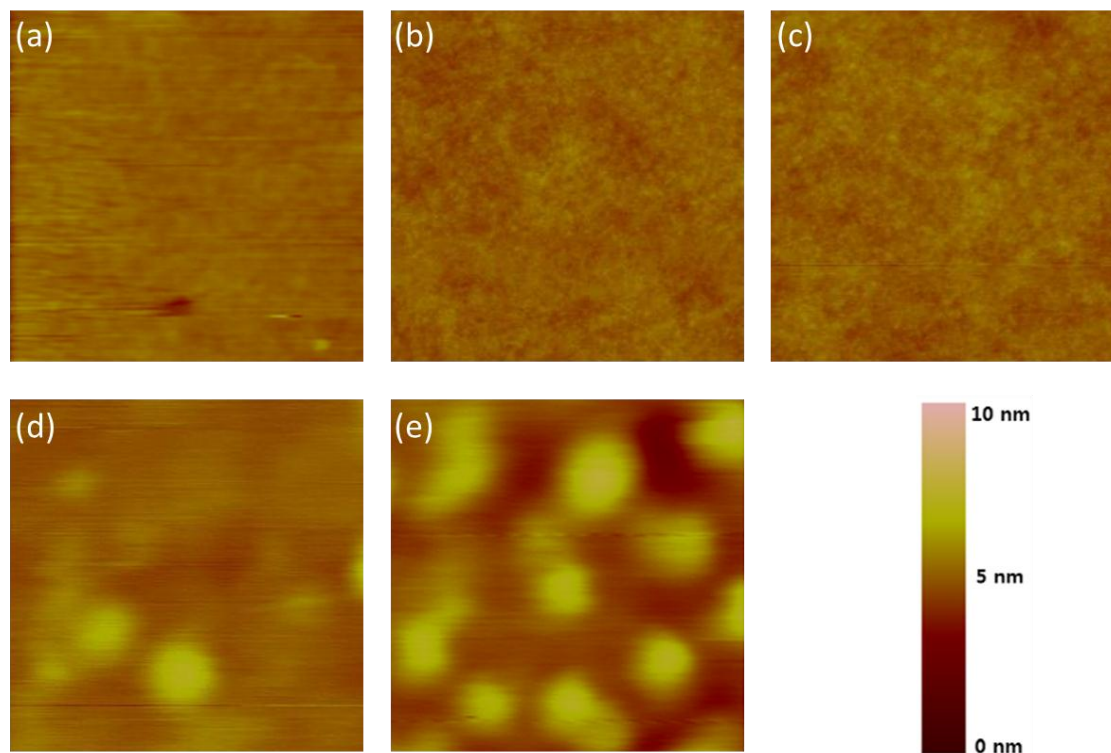


Figure 3.8. AFM height images ($1\ \mu\text{m} \times 1\ \mu\text{m}$ scale) of (a) pure PCBM film, (b) 1wt%, (c) 3 wt%, (d) 5 wt%, and (e) 10 wt% DMBI-doped PCBM film.

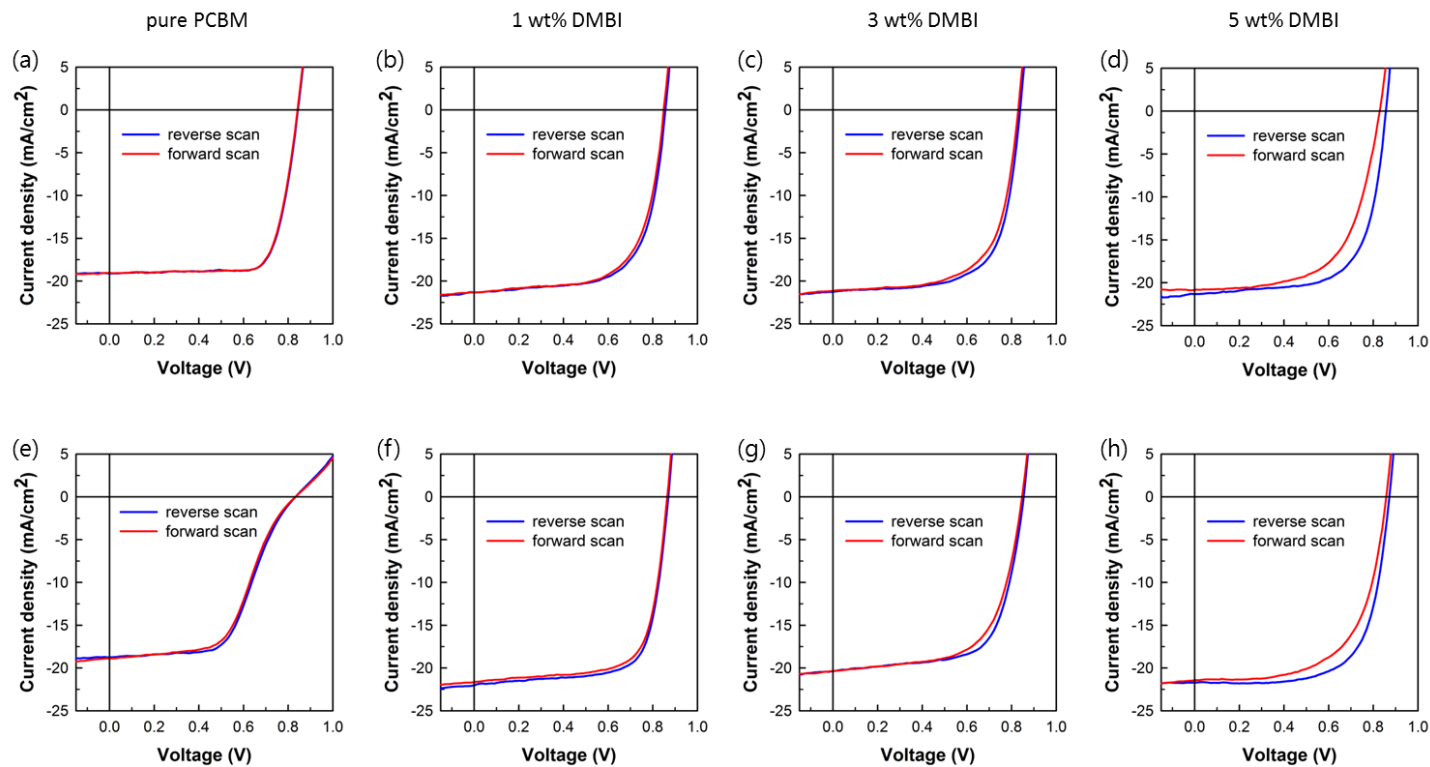


Figure 3.9. Hysteresis curves for devices with (a), (b), (c), (d) thin ETL, and (e), (f), (g), (h) thick ETL.

revealed that the pristine PCBM film and 1 wt% doped PCBM film have a smooth surface while PCBM films doped with 3 wt% and higher DMBI show a rough surface with large aggregates (Figure 3.8). The rough surface inevitably causes poor contact between the ETL and the cathode, resulting in the increase of series resistance (Table 3.1). Hence, excessive doping may worsen the device performance, especially decreasing the FF.

When we measure the hysteresis of devices, as shown in Figure 3.9, we realize that all devices exhibit stable $J-V$ curves without significant hysteresis with respect to the scan direction. However, the devices with high doping concentration (>3 wt%) exhibit weak hysteresis. Although the origin of the hysteresis has not clearly been identified, the trap sites, ferroelectric properties of perovskites and ion migration have been proposed as possible reasons. Hence, we have assumed that the hysteresis of our devices with high doping concentration is caused by an increase of trap sites due to DMBI doping.

To investigate the charge transfer between perovskite layer and ETL, transient photoluminescence measurement was conducted (Figure 3.10). $\text{CH}_3\text{NH}_3\text{PbI}_3/\text{PCBM}$ film and $\text{CH}_3\text{NH}_3\text{PbI}_3/\text{DMBI}$ -doped PCBM films were prepared on quartz glass. PL decays were fitted with bi-exponential decay curves to give the average lifetime of charge carriers (Table 3.3).^{47,85} While $\text{CH}_3\text{NH}_3\text{PbI}_3/\text{PCBM}$ film shows short average charge carrier lifetime of 2.2 ns, $\text{CH}_3\text{NH}_3\text{PbI}_3/\text{DMBI}$ -doped PCBM films show slightly increased charge carrier lifetimes of 3.0 ns, 5.3 ns, and 8.0 ns for 1 wt%, 3 wt%, and 5 wt% DMBI doped PCBM, respectively, as shown in Table 3.2. From these

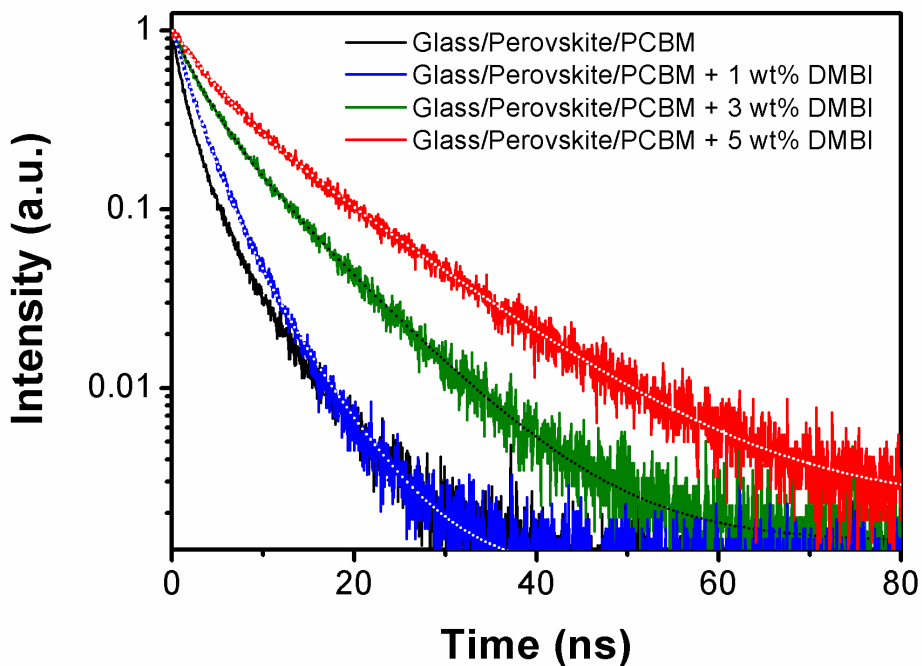


Figure 3.10. Transient Photoluminescence spectra for perovskite/pure PCBM film, and perovskite/DMBI-doped PCBM films with various dopant concentrations deposited on quartz glass.

results we can notice that excessive DMBI doping hinders effective charge transfer from $\text{CH}_3\text{NH}_3\text{PbI}_3$ to PCBM at the interface, results in the deterioration of solar cell performance. Increase of trap sites by DMBI aggregation and insufficient energy level offset between $\text{CH}_3\text{NH}_3\text{PbI}_3$ and highly doped PCBM due to the up-shifts of energy levels are possible

reasons for the decrease of solar cell performance. We conclude that, therefore, 1 wt% is the optimized dopant concentration between the increase of charge transporting property and the decrease of charge transfer property.

Table 3.3. Fitting parameters of PL decays shown in Figure 3.10.

Dopant conc. (wt%)	A_1	τ_1 (ns)	A_2	τ_2 (ns)	$\tau_{\text{ave}}^{[a]}$ (ns)
0	0.776	1.417	0.224	4.939	2.206
1	0.807	2.349	0.193	5.616	2.980
3	0.584	3.029	0.416	8.557	5.329
5	0.508	3.976	0.492	12.136	7.991

Fit function: $I(t) = A_1 \exp(-t/\tau_1) + A_2 \exp(-t/\tau_2)$

$$^{[a]} \tau_{\text{ave}} = A_1 \tau_1 + A_2 \tau_2$$

3.1.5 Summary

We first introduced an *n*-type dopant, DMBI, to dope the PCBM as an electron transporting material in planar heterojunction perovskite solar cells with inverted structure. PCBM was effectively *n*-doped by DMBI, which was evidenced by UV–Vis–NIR absorption and UPS measurements. In UV–Vis–NIR absorption spectra, additional absorption peak due to the formation of PCBM radical anion is observed. Fermi level up-shift of PCBM

with adding DMBI confirmed by UPS measurements proves effective *n*-doping is occurred by DMBI. Furthermore, the electrical conductivity of PCBM is greatly increased from 3.8×10^{-9} S/cm to 6.1×10^{-5} S/cm with 1 wt% DMBI doping. Solar cell devices with *n*-doped PCBM ETL exhibit higher PCE with remarkably increased J_{SC} as compared to un-doped device mainly due to the increased electrical conductivity, which enhances the electron transporting property. For the devices with 50-nm thick ETL, PCE is moderately increased from 12.3% ($J_{SC} = 19.1 \text{ mA cm}^{-2}$ and $V_{OC} = 0.84 \text{ V}$, FF = 0.77) to 13.0% ($J_{SC} = 21.0 \text{ mA cm}^{-2}$ and $V_{OC} = 0.85 \text{ V}$, FF = 0.73) with 1 wt% DMBI doping. For the devices with 105-nm thick ETL, meanwhile, PCE is notably increased from 8.9% ($J_{SC} = 19.6 \text{ mA cm}^{-2}$ and $V_{OC} = 0.83 \text{ V}$, FF = 0.55) to 13.8% ($J_{SC} = 22.0 \text{ mA cm}^{-2}$ and $V_{OC} = 0.87 \text{ V}$, FF = 0.72) with 1 wt% DMBI doping. The excessive doping with >1 wt% DMBI causes aggregation of DMBI, which increases trap sites, results in the deterioration of the solar cell performance. AFM images well exhibit the aggregation of DMBI and the increase of surface roughness. As a result of the aggregation of DMBI, *J*-*V* hysteresis and the average charge carrier lifetime of $\text{CH}_3\text{NH}_3\text{PbI}_3/\text{ETL}$ slightly increase with the increase of dopant concentration. Since the effect of DMBI-doping on photovoltaic performance is more prominent for the device with thicker PCBM layer, this method allows us to fabricate thicker ETL layer, which has a benefit of industrial processing of device fabrication. In short, this simple doping method can be an effective strategy for enhancing the performance of planar heterojunction perovskite solar cells with inverted structure.

3.2 Perylene diimide-based non-fullerene acceptors as electron transporting materials for inverted structure planar heterojunction perovskite solar cells and the performance enhancement by *n*-doping

3.2.1 Synthesis and characterization

Synthesis of $\text{CH}_3\text{NH}_3\text{I}$, fabrication of $\text{CH}_3\text{NH}_3\text{PbI}_3$ perovskite film, and synthesis of DMBI were conducted identically with section 3.1. Among non-fullerene electron acceptors developed for OPVs, NDI and perylene diimide (PDI) derivatives have mostly been used due to their easy synthesis, easy tunability of frontier energy levels, excellent thermal and photochemical stability, and strong electron accepting ability.^{43-46,53-55} In this study, we choose PDI dimer (diPDI) as ETL material of inverted perovskite solar cells because of ease of synthesis, excellent performance as electron acceptor, and similar energy level to PCBM.^{43,53} diPDI is synthesized through 3 steps with a moderate yield (Scheme 2.2). First, 3,4,9,10-perylenetetracarboxylic dianhydride is reacted with 4-heptylamine to yield PDI with 1-propylbutyl side group. Then, the PDI is brominated for dimerization. Finally, two mono-brominated PDIs are coupled by homo-coupling reaction to yield diPDI. Synthesized molecules of each step were confirmed by ^1H NMR (Figure 3.11-3.13).

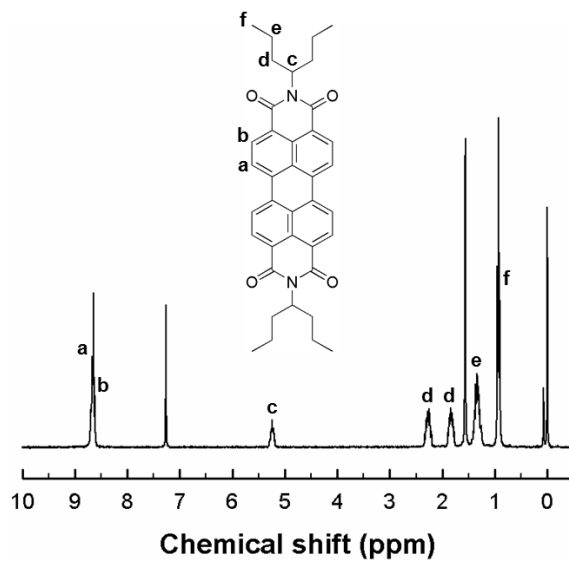


Figure 3.11. ¹H NMR spectrum of PDI monomer (compound **2** in Scheme 2.2).

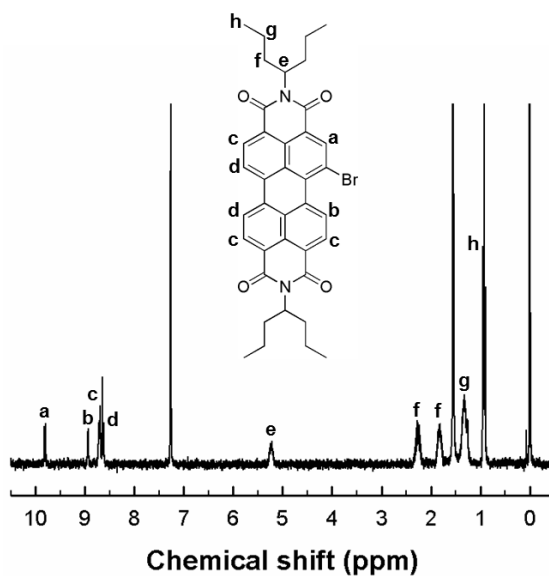


Figure 3.12. ¹H NMR spectrum of mono-brominated PDI monomer (compound **3** in Scheme 2.2).

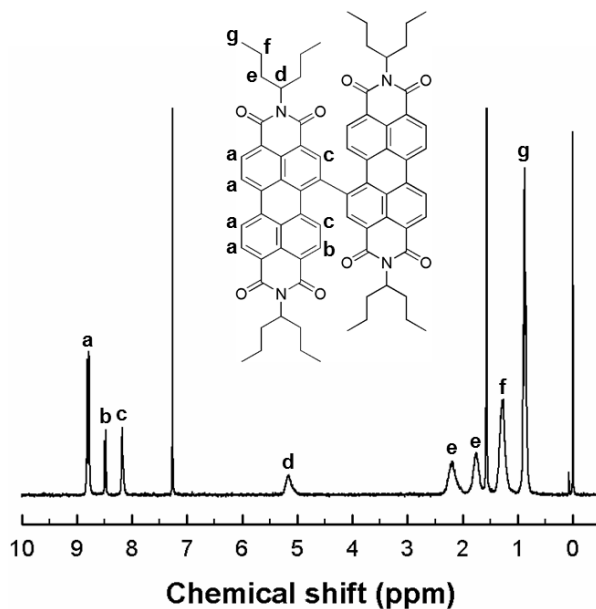


Figure 3.13. ^1H NMR spectrum diPDI.

3.2.2 Charge transfer characteristics

When photoluminescence (PL) spectra are measured to evaluate the suitability of diPDI as ETL material for inverted perovskite solar cell, as shown in Figure 3.14, the emission peak of perovskite ($\text{CH}_3\text{NH}_3\text{PbI}_3$) at 780 nm is effectively quenched by diPDI as effective as by PCBM, indicating that the charge transfer from perovskite to diPDI takes place effectively at the $\text{CH}_3\text{NH}_3\text{PbI}_3/\text{diPDI}$ interface.

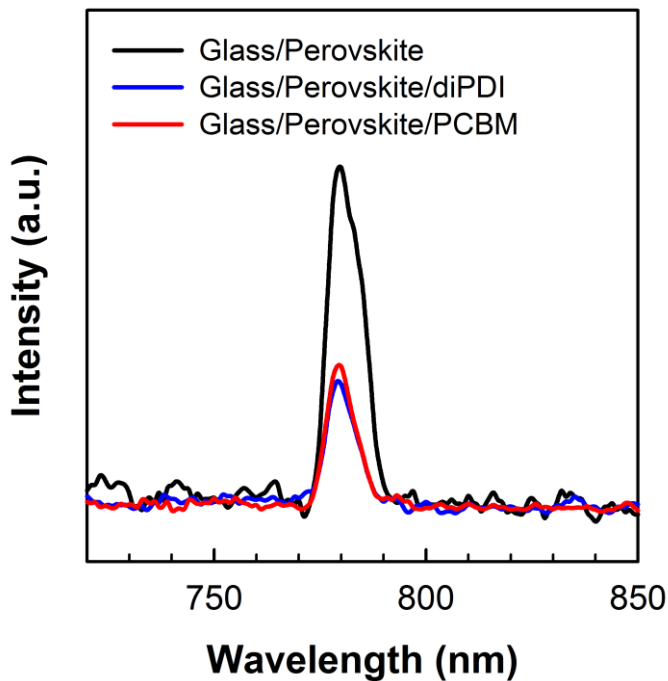


Figure 3.14. Photoluminescence spectra for pristine perovskite, perovskite/diPDI, and perovskite/PCBM films deposited on quartz glass (excited at 520 nm).

Transient PL (trPL) was also measured to examine the average charge carrier lifetimes (Figure 3.15). PL decays were fitted with bi-exponential decay curves to give the lifetime of carriers and the fitting parameters are displayed in Table 3.4. Pristine perovskite film shows average charge carrier lifetime of 38.7 ns, while perovskite/diPDI, perovskite/PCBM films

exhibit notably reduced average lifetimes of 1.2 ns and 2.2 ns, respectively. These reduced charge carrier lifetimes of $\text{CH}_3\text{NH}_3\text{PbI}_3/\text{ETL}$ than that of pristine $\text{CH}_3\text{NH}_3\text{PbI}_3$ film imply that electrons generated in the $\text{CH}_3\text{NH}_3\text{PbI}_3$ film are effectively transferred to the ETL at the interface. This result leads us to expect that diPDI exhibits the photovoltaic performance comparable to PCBM as an ETL material of inverted perovskite solar cells.

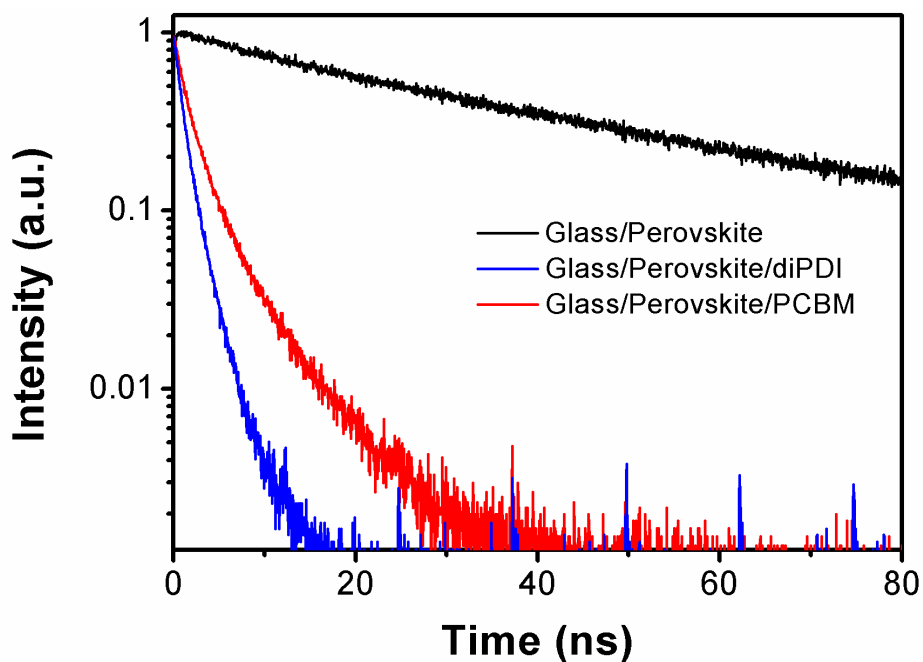


Figure 3.15. Transient PL spectra for pristine perovskite, perovskite/diPDI, and perovskite/PCBM films deposited on quartz glass.

Table 3.4. Fitting parameters of PL decays shown in Figure 3.15.

Quencher	A_1	τ_1 (ns)	A_2	τ_2 (ns)	$\tau_{\text{ave}}^{[a]}$ (ns)
-	0.783	45.964	0.217	12.590	38.722
diPDI	0.903	1.035	0.097	3.075	1.233
PCBM	0.776	1.417	0.224	4.939	2.206

Fit function: $I(t) = A_1 \exp(-t/\tau_1) + A_2 \exp(-t/\tau_2)$

$$^{[a]} \tau_{\text{ave}} = A_1 \tau_1 + A_2 \tau_2$$

3.2.3 Photovoltaic properties

Solar cell devices with diPDI as ETL material are fabricated with an inverted configuration of ITO/PEDOT:PSS/CH₃NH₃PbI₃/diPDI/TiO₂/Al. The frontier energy levels of each layer are shown in Figure 3.16. Stepwise alignment of energy levels from CH₃NH₃PbI₃ layer to Al cathode may facilitate transport and collection of electrons. The device with diPDI as ETL exhibits a moderate PCE of 7.1% in current density–voltage curve (see Figure 3.17a and Table 3.5). The moderate PCE is attributed to low electrical conductivity of diPDI (4.7×10^{-12} S/cm), which results in poor charge transport in diPDI layer although the charge transfer at the CH₃NH₃PbI₃/diPDI interface is effective. In our previous study, we have

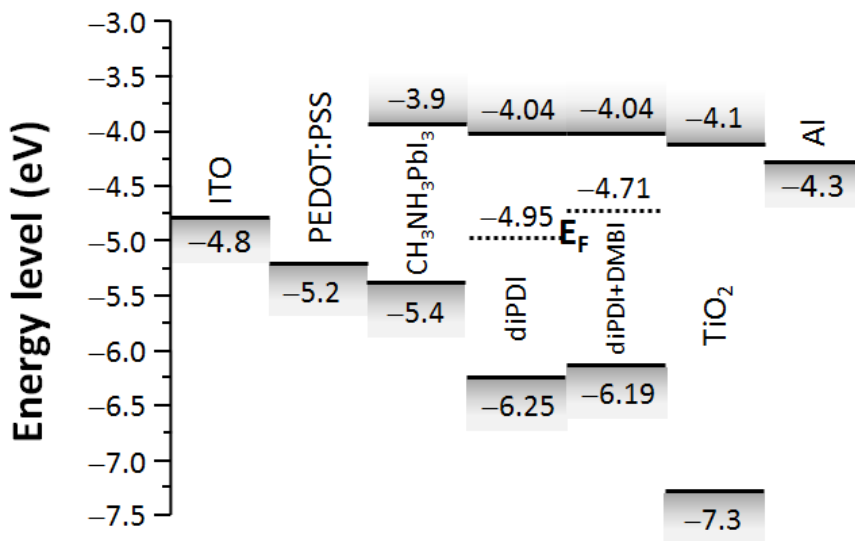


Figure 3.16. Energy levels of each layer of photovoltaic devices.

found that the electrical conductivity of PCBM is remarkably enhanced upon *n*-doping by DMBI (from 3.8×10^{-9} S/cm to 6.1×10^{-5} S/cm) and thereby the PCE of solar cells is increased from 8.9% to 13.8%.⁸⁶ Similarly, when we add 1 wt% of DMBI to diPDI, the electrical conductivity of diPDI is increased from 4.7×10^{-12} S/cm to 7.6×10^{-8} S/cm.

As the amount of DMBI added to diPDI is increased, the PCE of solar cell device increases first and then decreases showing a maximum at 1 wt% addition (see Figure 3.17a and Table 3.5). When diPDI is doped by 1 wt% of DMBI, the cell exhibits the maximum PCE of 10.0% with a J_{SC} of 21.6 mA cm^{-2} , a V_{OC} of 0.86 V and a FF of 0.54. Especially, J_{SC} is largely increased

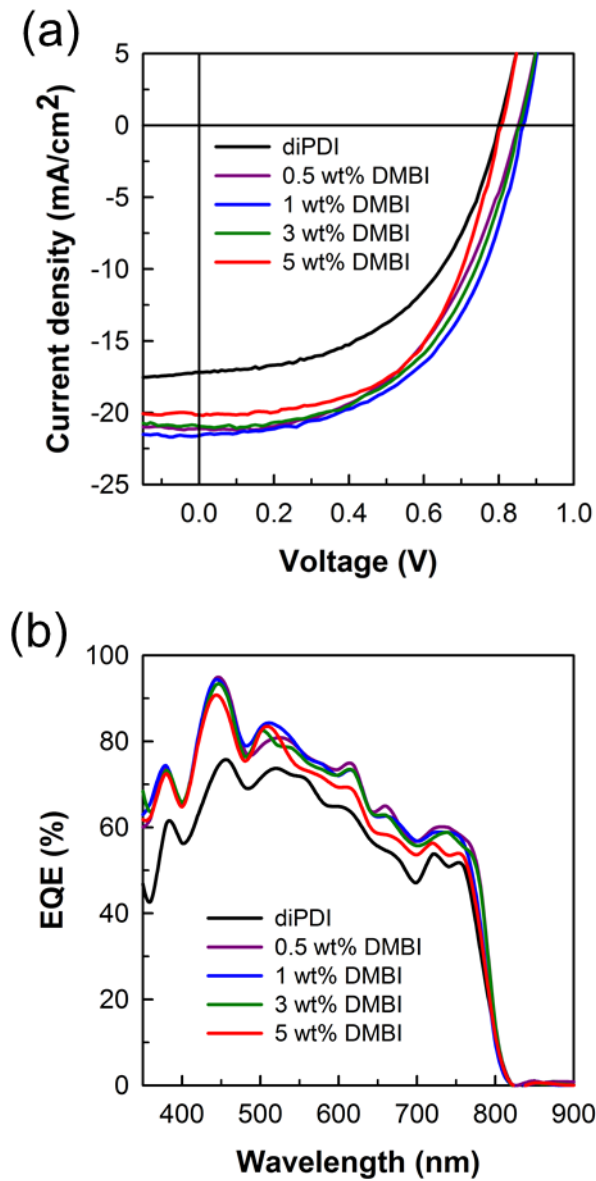


Figure 3.17. (a) *J-V* curves, and (b) EQE spectra of the devices with pure diPDI and DMBI-doped diPDI with various dopant concentrations as ETL.

Table 3.5. Photovoltaic performances of devices with diPDI with different dopant (DMBI) concentrations as ETL.

Dopant conc. (wt%)	J_{SC} (mA cm ⁻²)	V_{OC} (V)	FF	PCE ^a (%)	R_{sh}^b (Ω cm ²)	R_s^b (Ω cm ²)
0.0	17.2	0.80	0.51	7.1 (6.6)	447	9.7
0.5	21.1	0.85	0.51	9.2 (8.7)	571	9.7
1.0	21.6	0.86	0.54	10.0 (9.3)	526	7.2
3.0	21.0	0.85	0.54	9.6 (9.1)	555	8.7
5.0	20.2	0.81	0.54	8.8 (8.4)	559	8.7

^aAverage PCE values based on at least 10 devices are indicated in parentheses.

^bThe series and shunt resistance were calculated by the slopes of J - V curves.

upon *n*-doping due to an increased electrical conductivity of diPDI layer. Further addition of DMBI above 1% decreases the photovoltaic performance probably due to aggregation of DMBI.^{49,86} External quantum efficiency (EQE) spectra also demonstrate the effect of *n*-doping on the current density (Figure 3.17b). The devices with *n*-doped diPDI as ETL show higher EQE values than the device with un-doped diPDI as ETL.

3.2.4 Characterization of *n*-doping

To characterize the effect of *n*-doping, UV–Vis–NIR absorption and ultraviolet photoelectron spectroscopy (UPS) were measured (Figure 3.18 and 3.19). Absorption spectra of DMBI-doped diPDI films show additional peaks around 700 nm and 800 nm, as shown in Figure 3.18, while the peak intensity increases with the doping concentration, indicating that DMBI effectively dopes diPDI by donating an electron to diPDI to form diPDI radical anions.⁸⁷⁻⁸⁸ When the Fermi level and the HOMO energy level of diPDI were measured by UPS, the Fermi level of diPDI is up-shifted from -4.95 eV to -4.71 eV upon 1 wt% addition of DMBI, and further addition of DMBI up-shifts further the Fermi level up to -4.61 eV at 5 wt% addition. The up-shift of the Fermi level of diPDI upon addition of DMBI is a definite evidence of *n*-doping, while the HOMO energy level of diPDI is not significantly changed, as clearly demonstrated in Figure 3.16. Here, the work function is determined by subtracting the binding energy cutoffs in high binding energy region (Figure 3.19a) from the He I photon energy (21.22

eV), and the energy gap between the Fermi level and the HOMO energy level is determined from the binding energy cutoffs in low binding energy region (Figure 3.19b). In short, the addition of a small amount of DMBI effectively dopes diPDI to form diPDI radical anion, increasing the electrical conductivity, which enhances the electron transporting property of diPDI.

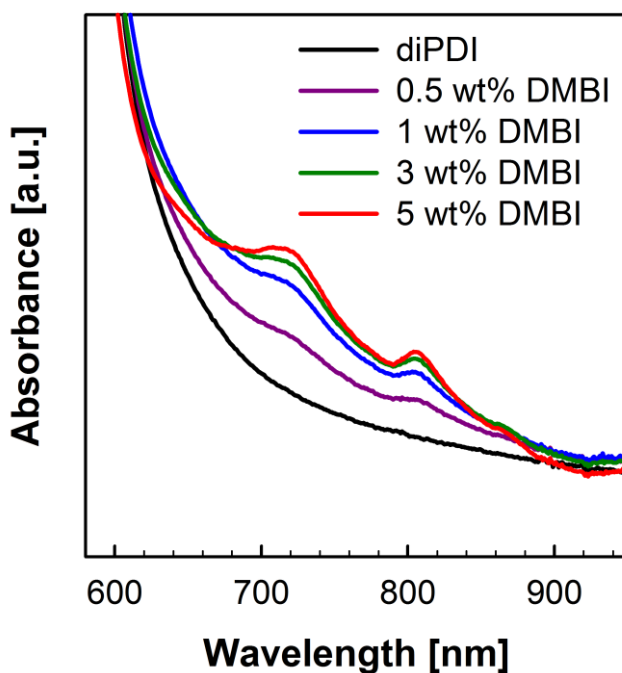


Figure 3.18. UV-Vis-NIR absorption spectra of pure diPDI film and DMBI-doped diPDI films with various dopant concentrations. All films are fabricated by spin-coating the chlorobenzene solution on glass.

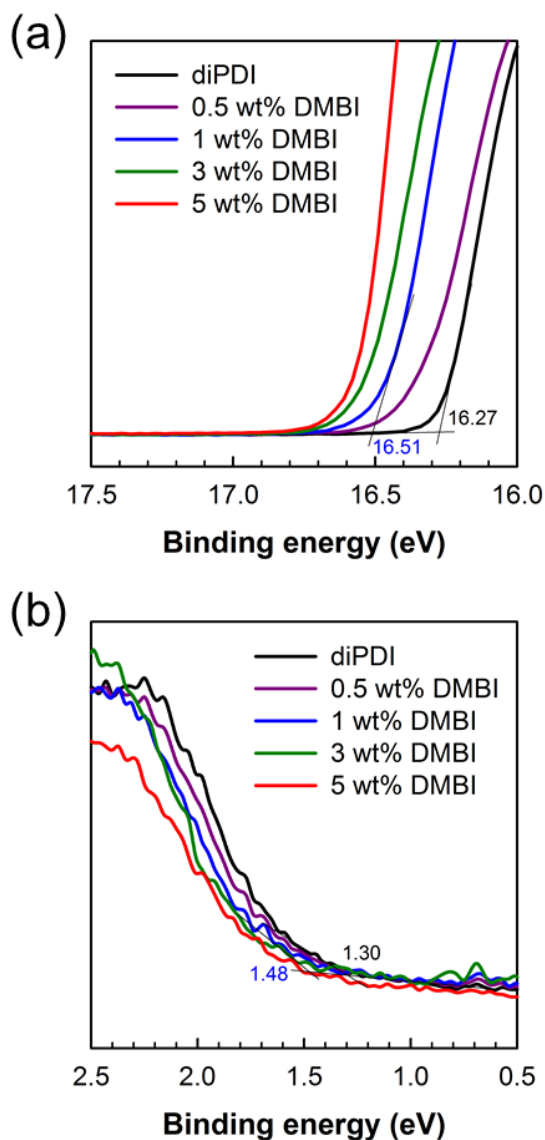


Figure 3.19. UPS spectra of pure diPDI and DMBI-doped diPDI with various dopant concentrations in (a) high binding energy region and (b) low binding energy region. Binding energy cutoffs of pure diPDI and diPDI doped with 1 wt% DMBI are indicated.

3.2.5 Effects of excessive doping on photovoltaic properties

When the $J-V$ hysteresis curves of the devices are examined (Figure 3.20), all devices exhibit moderately stable hysteresis while stronger hysteresis is observed at higher doping concentration. Since it has been reported that one of possible reasons for hysteresis is the charge accumulation at the interface, we have assumed that the hysteresis of our device with high doping concentration is caused by an increase of trap sites and accumulated charges due to aggregation of DMBI.^{74,89}

To identify the charge transfer characteristics between perovskite layer and diPDI ETL, transient photoluminescence spectra was measured (Figure 3.21). $\text{CH}_3\text{NH}_3\text{PbI}_3/\text{diPDI}$ film and $\text{CH}_3\text{NH}_3\text{PbI}_3/\text{DMBI-doped diPDI}$ films were prepared on quartz glass. PL decays were fitted with bi-exponential decay curves to give the average lifetime of charge carriers (Table 3.6). While $\text{CH}_3\text{NH}_3\text{PbI}_3/\text{diPDI}$ film shows short average charge carrier lifetime of 1.2 ns, $\text{CH}_3\text{NH}_3\text{PbI}_3/\text{DMBI-doped diPDI}$ films show slightly increased charge carrier lifetimes of 2.6 ns, 3.3 ns, 4.7 ns, and 6.0 ns for 0.5 wt%, 1 wt%, 3 wt%, and 5 wt% DMBI doped diPDI, respectively, as shown in Table 3.6. We confirmed that, from these results, excessive doping of DMBI hampers effective charge transfer from $\text{CH}_3\text{NH}_3\text{PbI}_3$ to diPDI at the $\text{CH}_3\text{NH}_3\text{PbI}_3/\text{diPDI}$ interface, results in the deterioration of solar cell performance. Increase of trap sites by DMBI aggregation and insufficient energy gap between $\text{CH}_3\text{NH}_3\text{PbI}_3$ and highly doped diPDI due to the up-shifts of energy levels are probable reasons for the decrease of solar cell

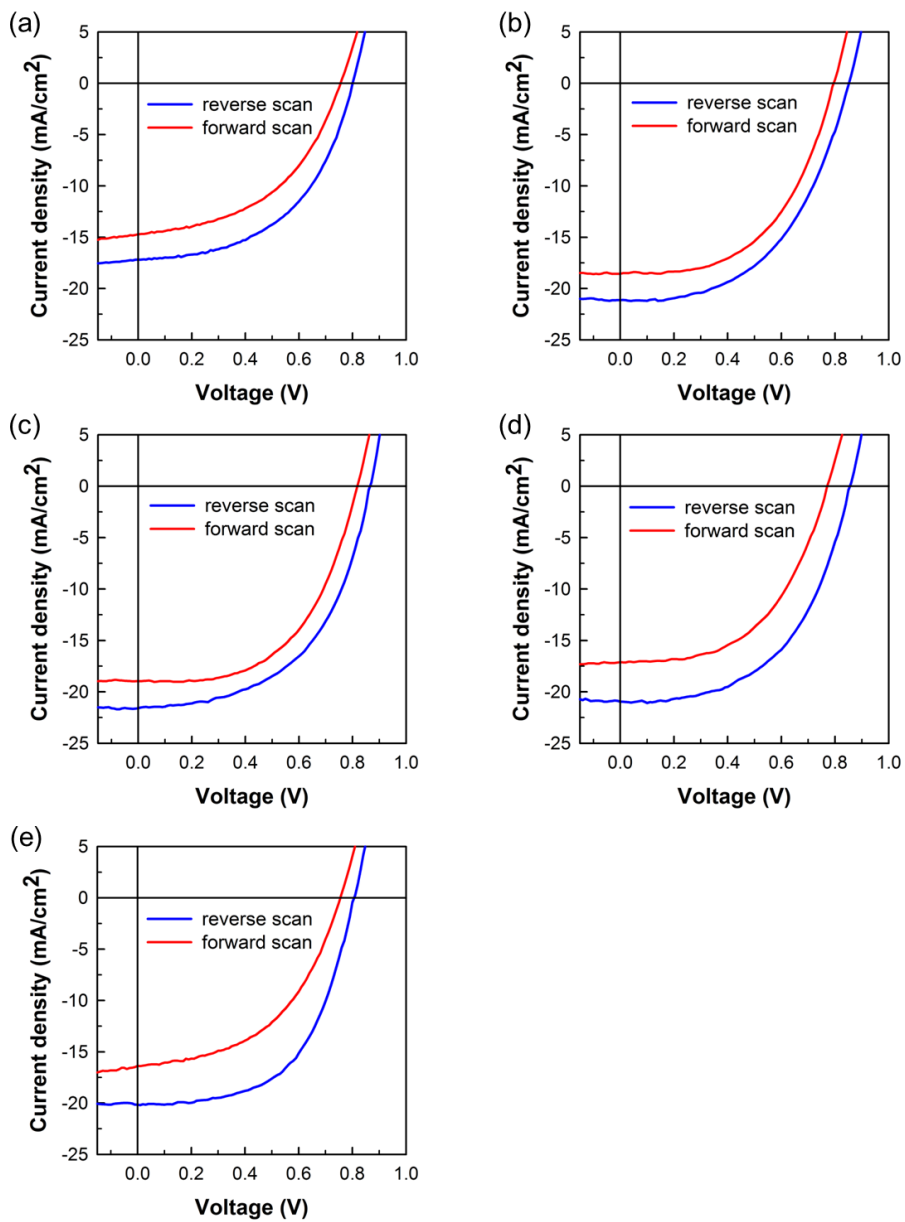


Figure 3.20. Hysteresis curves for devices with (a) pure diPDI, (b) 0.5 wt% DMBI-doped diPDI, (c) 1 wt% DMBI-doped diPDI, (d) 3 wt% DMBI-doped diPDI, and (e) 5 wt% DMBI-doped diPDI.

performance. Therefore we conclude that 1 wt% is the optimized dopant concentration, which is the same result with the case of PCBM ETL, between the increase of charge transporting property and the decrease of charge transfer property.

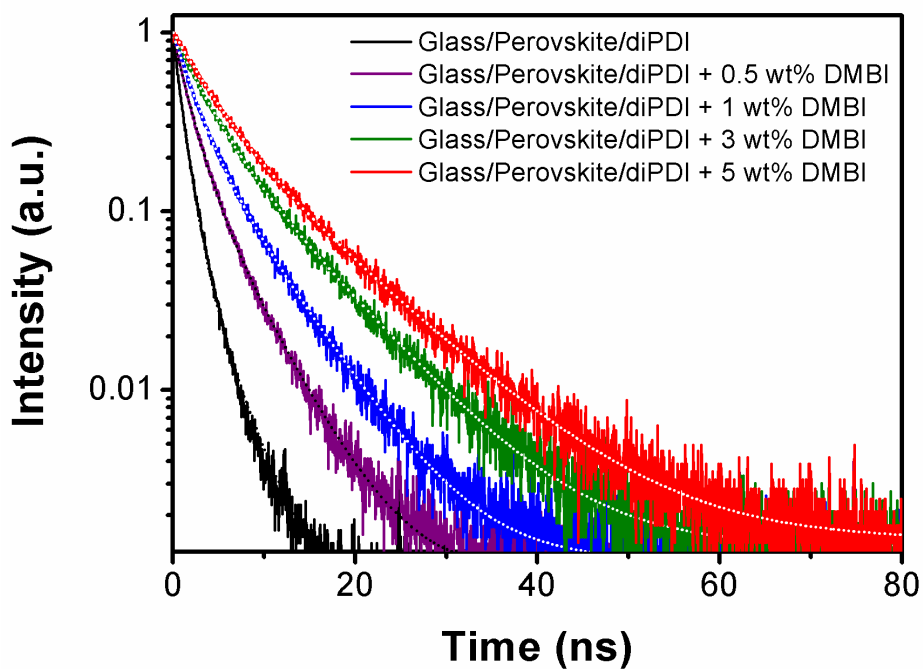


Figure 3.21. Transient Photoluminescence spectra for perovskite/pure diPDI film, and perovskite/DMBI-doped diPDI films with various dopant concentrations deposited on quartz glass.

Table 3.6. Fitting parameters of PL decays shown in Figure 3.21.

Dopant conc. (wt%)	A_1	τ_1 (ns)	A_2	τ_2 (ns)	$\tau_{\text{ave}}^{[a]}$ (ns)
0.0	0.903	1.035	0.097	3.075	1.233
0.5	0.897	2.301	0.103	4.714	2.550
1.0	0.668	2.092	0.332	5.783	3.317
3.0	0.642	2.947	0.358	7.808	4.687
5.0	0.609	3.642	0.391	9.568	5.959

Fit function: $I(t) = A_1 \exp(-t/\tau_1) + A_2 \exp(-t/\tau_2)$

$$^{[a]} \tau_{\text{ave}} = A_1 \tau_1 + A_2 \tau_2$$

3.2.6 PDI monomer as ETL material

PDI monomer is well-known *n*-type electron accepting material as well as diPDI. While the synthesis of diPDI requires 3 steps include mono-bromination and dimerization of PDI with relatively low yield (32% and 36%, respectively), PDI monomer can be simply synthesized by an alkylation step with high yield (86%) (See section 2.1.6 and Scheme 2.2).

When the current density–voltage curves of perovskite solar cells are measured with an inverted device configuration of ITO/PEDOT:PSS/CH₃NH₃PbI₃/PDI or PDI:DMBI/TiO₂/Al, J_{SC} is

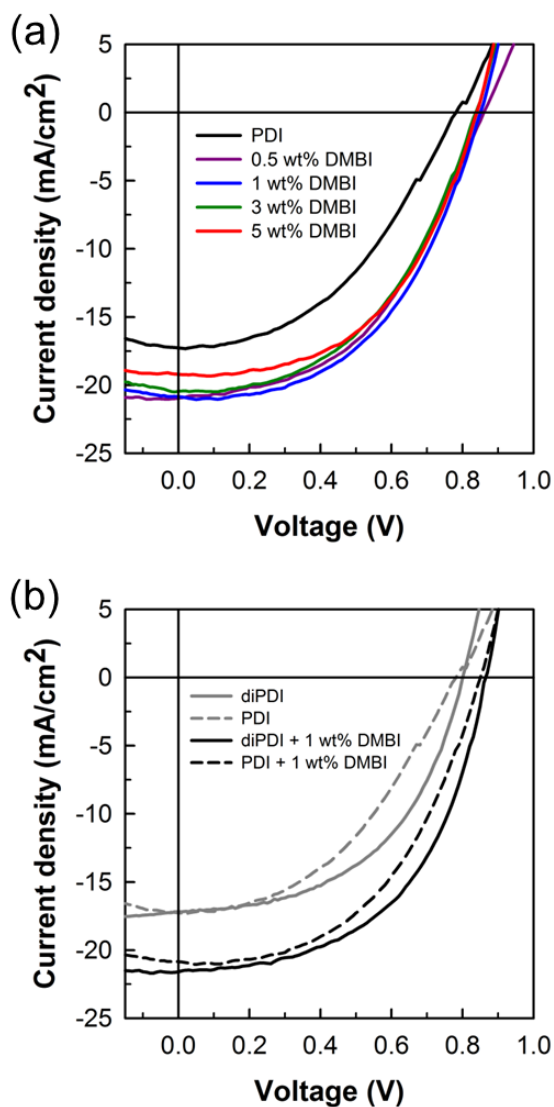


Figure 3.22. (a) $J-V$ curves of the devices with pure PDI and DMBI-doped PDI with various dopant concentrations as ETL, and (b) comparison of device performance between diPDI and PDI monomer with un-doped and optimized (1 wt% of DMBI doped) devices.

Table 3.7. Photovoltaic performances of devices with PDI with different dopant (DMBI) concentrations as ETL.

Dopant conc. (wt%)	J_{SC} (mA cm ⁻²)	V_{OC} (V)	FF	PCE ^a (%)	R_{sh}^b (Ω cm ²)	R_s^b (Ω cm ²)
0.0	17.2	0.79	0.44	6.0 (5.7)	528	25.8
0.5	21.0	0.86	0.47	8.5 (8.0)	540	21.1
1.0	20.9	0.85	0.50	8.9 (8.5)	571	18.0
3.0	20.5	0.84	0.48	8.2 (7.9)	542	18.8
5.0	19.2	0.84	0.50	8.1 (7.7)	568	17.9

^aAverage PCE values based on at least 10 devices are indicated in parentheses.

^bThe series and shunt resistance were calculated by the slopes of J - V curves.

remarkably enhanced by the addition of DMBI, as shown in Figure 3.22a and Table 3.7, which is similar result with the case of diPDI. The PCE is increased from 6.0% with a J_{SC} of 17.2 mA cm^{-2} to 8.9% with a J_{SC} of 20.9 mA cm^{-2} , when 1 wt% DMBI is added. Although the overall efficiencies are relatively low, the effectiveness of *n*-doping strategy is proved one more time.

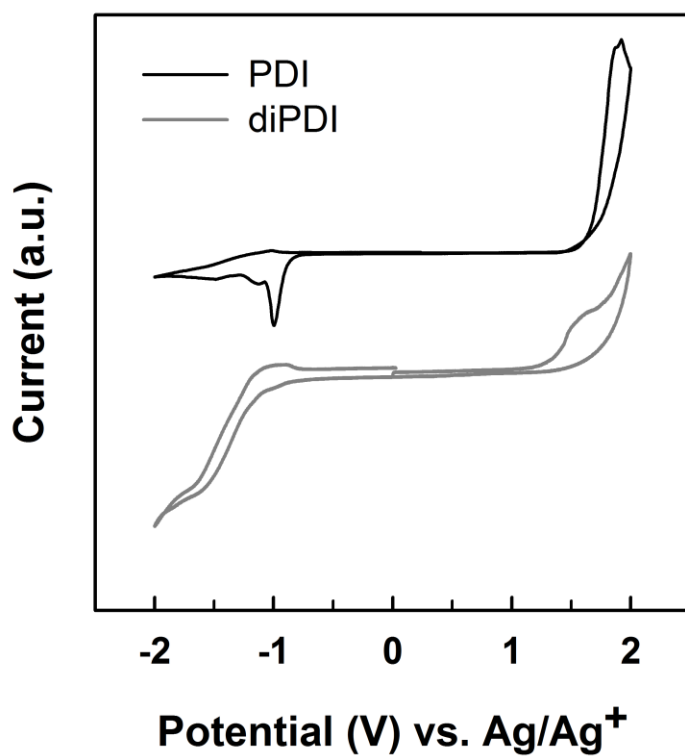


Figure 3.23. Cyclic voltammograms of PDI monomer and diPDI

When we compare the devices with PDI ETL to the devices with diPDI ETL, as shown in Figure 3.22b, solar cell performances of the devices with PDI ETL are worse than the devices with diPDI ETL, mainly due to the increase of series resistance (R_s) and the resultant decrease of FF (See Table 3.4 and Table 3.7). We have assumed that the decrease of device performance is mainly due to the inappropriate energy level of PDI monomer. When the electrochemical properties of PDI and diPDI are measured by cyclic voltammetry, as shown in Figure 3.23, the HOMO and LUMO energy levels of PDI monomer are -6.68 eV and -4.16 eV, respectively, while those of diPDI are -6.37 eV and -3.99 eV, respectively. Because the LUMO energy level of PDI monomer (-4.16 eV) is too deep to effectively transfer electron from PDI to TiO_2 (LUMO energy level = -4.10 eV, see Figure 3.16) at the PDI/ TiO_2 interface, the devices with PDI ETL exhibit quite high series resistances and relatively low solar cell efficiencies.

3.2.7 Summary

We first introduced a solution processible perylene diimide-based non-fullerene electron transporting material, diPDI, for inverted perovskite solar cells with planar heterojunction architecture. As an alternative to PCBM, diPDI shows electron accepting ability comparable to PCBM, which is evidenced by time-independent photoluminescence quenching. Transient PL also exhibits that charge transfer at the $\text{CH}_3\text{NH}_3\text{PbI}_3/\text{diPDI}$ interface occurs effectively as well as at the $\text{CH}_3\text{NH}_3\text{PbI}_3/\text{PCBM}$ interface. The solar cell

device with diPDI as non-fullerene electron transporting material exhibits a moderate PCE of 7.1% with J_{SC} of 17.2 mA cm^{-2} , V_{OC} of 0.80 V, and FF of 0.51. Furthermore, when diPDI is doped by 1 wt% DMBI, the efficiency of device with the DMBI-doped diPDI as ETL is remarkably increased to 10.0% with J_{SC} of 21.6 mA cm^{-2} , V_{OC} of 0.86 V, and FF of 0.54. This enhancement is attributed mainly to the increased electrical conductivity of diPDI and up-shift of the Fermi level of diPDI by *n*-doping. The electrical conductivity of diPDI is greatly increased from $4.7 \times 10^{-12} \text{ S/cm}$ to $7.6 \times 10^{-8} \text{ S/cm}$ with 1 wt% DMBI doping. Effective *n*-doping of diPDI by DMBI was proved by UV–Vis–NIR absorption and UPS measurements. UV–Vis–NIR absorption spectra show the additional peaks as a result of formation of diPDI radical anion. Besides, Fermi level of diPDI is up-shifted from -4.95 eV to -4.71 eV with 1 wt% of DMBI, indicative of effective *n*-doping. The excessive doping with $>1 \text{ wt\%}$ DMBI causes aggregation of DMBI, which increases trap sites, results in the deterioration of the solar cell performance. As a result of the aggregation of DMBI, *J*–*V* hysteresis behavior emerges, and the average charge carrier lifetime of $\text{CH}_3\text{NH}_3\text{PbI}_3/\text{ETL}$ slightly increases, with the increase of DMBI concentration. We introduce a PDI monomer, as well as diPDI, to perovskite solar cells as ETL material. While the synthesis of PDI monomer is much easier than that of PDI dimer, the solar cell devices with PDI ETL exhibit relatively poor performances. The PCE is increased from 6.0% to 8.9% with 1 wt% DMBI doping. The reason why the solar cell devices with PDI ETL show worse performance than the devices with diPDI ETL is an inadequate energy level of PDI monomer. PDI

has LUMO energy level of -4.16 eV, as observed by cyclic voltammetry, which is deeper than the LUMO energy level of TiO_2 . As a result, the devices with PDI ETL show high series resistances and low FF. These overall results lead us to conclude that perylene diimide-based non-fullerene acceptor is a promising electron transporting material for inverted perovskite solar cells when *n*-doped by DMBI. This study motivates us to pursue development of effective non-fullerene electron acceptors for high performance perovskite solar cells.

Chapter 4. Conclusions

In this work, we introduced an *n*-type dopant, DMBI, to effectively dope electron transporting materials include PCBM and non-fullerene acceptors, for achieving high performance of planar heterojunction perovskite solar cells with inverted structure.

First, we primarily used an *n*-type dopant, DMBI, to dope the PCBM as an electron transporting material in planar heterojunction perovskite solar cells. PCBM was effectively *n*-doped by DMBI, which was evidenced by UV–Vis–NIR absorption and UPS measurements. In UV–Vis–NIR absorption spectra, additional absorption peak is clearly observed as a result of the formation of PCBM radical anion. Fermi level up-shifts of PCBM with increasing concentration of DMBI confirmed by UPS measurements prove that effective *n*-doping of PCBM is occurred by simple mixing with DMBI. Furthermore, the electrical conductivity of PCBM is greatly increased from 3.8×10^{-9} S/cm to 6.1×10^{-5} S/cm with 1 wt% DMBI doping. Solar cell devices with *n*-doped PCBM ETL exhibit higher PCE with remarkably increased J_{SC} as compared to un-doped device mainly due to the increased electrical conductivity, which enhances the electron transporting property. For the devices with 50-nm thick ETL, PCE is moderately increased from 12.3% ($J_{SC} = 19.1$ mA cm⁻² and $V_{OC} = 0.84$ V, FF = 0.77) to 13.0% ($J_{SC} = 21.0$ mA cm⁻² and $V_{OC} = 0.85$ V, FF = 0.73) with 1 wt% DMBI doping. For the devices with 105-nm thick ETL, meanwhile, PCE is notably increased from 8.9% ($J_{SC} =$

19.6 mA cm⁻² and $V_{OC} = 0.83$ V, FF = 0.55) to 13.8% ($J_{SC} = 22.0$ mA cm⁻² and $V_{OC} = 0.87$ V, FF = 0.72) with 1 wt% DMBI doping. Excessive doping with >1 wt% DMBI causes aggregation of DMBI, which increases trap sites, results in the deterioration of the solar cell performance. We recognized the aggregation of DMBI and the increase of surface roughness through AFM height measurements. As a result of the aggregation of DMBI, $J-V$ hysteresis and the average charge carrier lifetime of CH₃NH₃PbI₃/ETL slightly increase with the increase of dopant concentration. Since the effect of DMBI-doping on photovoltaic performance is more prominent for the device with thicker PCBM layer, this method allows us to fabricate thicker ETL layer, which has a benefit of industrial processing of device fabrication.

Second, we first introduced a solution processible perylene diimide-based non-fullerene electron transporting material, diPDI, for inverted perovskite solar cells with planar heterojunction architecture. As an alternative to PCBM, diPDI shows electron accepting ability comparable to PCBM, which is evidenced by time-independent photoluminescence quenching. Transient PL also exhibits that charge transfer at the CH₃NH₃PbI₃/diPDI interface occurs effectively as well as at the CH₃NH₃PbI₃/PCBM interface. The solar cell device with diPDI as non-fullerene electron transporting material exhibits a moderate PCE of 7.1% with J_{SC} of 17.2 mA cm⁻², V_{OC} of 0.80 V, and FF of 0.51. Furthermore, when diPDI is doped by 1 wt% DMBI, the efficiency of device with the DMBI-doped diPDI as ETL is remarkably increased to 10.0% with J_{SC} of 21.6 mA cm⁻², V_{OC} of 0.86 V, and FF of 0.54. This enhancement is attributed mainly to the increased electrical conductivity of diPDI and up-shift

of the Fermi level of diPDI by *n*-doping. The electrical conductivity of diPDI is greatly increased from 4.7×10^{-12} S/cm to 7.6×10^{-8} S/cm with 1 wt% DMBI doping. Effective *n*-doping of diPDI by DMBI was proved by UV–Vis–NIR absorption and UPS measurements. UV–Vis–NIR absorption spectra show the additional peaks as a result of formation of diPDI radical anion. Besides, Fermi level of diPDI is up-shifted from -4.95 eV to -4.71 eV with 1 wt% of DMBI, indicative of effective *n*-doping. The excessive doping with >1 wt% DMBI causes aggregation of DMBI, which increases trap sites, results in the deterioration of the solar cell performance. As a result of the aggregation of DMBI, *J–V* hysteresis behavior emerges, and the average charge carrier lifetime of $\text{CH}_3\text{NH}_3\text{PbI}_3/\text{ETL}$ slightly increases, with the increase of DMBI concentration. In addition, we introduce a PDI monomer, as well as diPDI, to perovskite solar cells as ETL material. While the synthesis of PDI monomer is much easier than that of PDI dimer, the solar cell devices with PDI ETL exhibit relatively poor performances. The PCE is increased from 6.0% to 8.9% with 1 wt% DMBI doping. The reason why the solar cell devices with PDI ETL show worse performance than the devices with diPDI ETL is an inadequate energy level of PDI monomer. PDI has LUMO energy level of -4.16 eV, as observed by cyclic voltammetry, which is deeper than the LUMO energy level of TiO_2 . As a result, the devices with PDI ETL show high series resistances and low FF. These overall results lead us to conclude that perylene diimide-based non-fullerene acceptor is a promising electron transporting material for inverted perovskite solar cells when *n*-doped by DMBI. This study motivates us to pursue development of effective non-fullerene electron

acceptors for high performance perovskite solar cells.

In short, we successfully introduced *n*-type dopant to ETL of planar heterojunction perovskite solar cells. We also used PDI-based non-fullerene acceptors as ETL materials with an appropriate doping. Device performance is enhanced mainly due to the increased electrical conductivity of ETL materials with effective *n*-doping. This simple *n*-doping method can be an effective strategy for enhancing the performance of perovskite solar cells.

Bibliography

- (1) Knittle, E.; Jeanloz, R. *Science* **1987**, *235*, 668.
- (2) Cheng, Z.; Lin, J. *CrystEngComm*. **2010**, *12*, 2646.
- (3) Pena, M. A.; Fierro, J. L. G. *Chem. Rev.* **2001**, *101*, 1981.
- (4) Weber, D. Z. *Naturforsch.* **1978**, *33b*, 1443.
- (5) Kojima, A.; Teshima, K.; Shirai, Y.; Miyasaka, T. *J. Am. Chem. Soc.* **2009**, *131*, 6050.
- (6) Stranks, S. D.; Eperon, G. E.; Grancini, G.; Menelaou, C.; Alcocer, M. J. P.; Leijtens, T.; Herz, L. M.; Petrozza, A.; Snaith, H. J. *Science* **2013**, *342*, 341.
- (7) Edri, E.; Kirmayer, S.; Henning, A.; Mukhopadhyay, S.; Gartsman, K.; Rosenwaks, Y.; Hodes, G.; Cahen, D. *Nano Lett.* **2014**, *14*, 1000.
- (8) Im, J. -H.; Lee, C. -R.; Lee, J. -W.; Park, S. -W.; Park, N. -G. *Nanoscale* **2011**, *3*, 4088.
- (9) Green, M. A.; Ho-Baillie, A.; Snaith, H. J. *Nat. Photonics* **2014**, *8*, 506.
- (10) Leijtens, T.; Stranks, S. D.; Eperon, G. E.; Lindblad, R.; Johansson, E. M. J.; McPherson, I. J.; Rensmo, H.; Ball, J. M.; Lee, M. M.; Snaith, H. J. *ACS Nano* **2014**, *8*, 7147.

- (11) Oga, H.; Saeki, A.; Ogomi, Y.; Hayase, S.; Seki, S. *J. Am. Chem. Soc.* **2014**, *136*, 13818.
- (12) Eperon, G. E.; Stranks, S. D.; Menelaou, C.; Johnston, M. B.; Herz, L. M.; Snaith, H. J. *Energy Environ. Sci.* **2014**, *7*, 982.
- (13) Green, M. A. *Prog. Photovolt: Res. Appl.* **2009**, *17*, 183.
- (14) Barnett, A.; Kirkpatrick, D.; Honsberg, C.; Moore, D.; Wanlass, M.; Emery, K.; Schwartz, R.; Carlson, D.; Bowden, S.; Aiken, D.; Gray, A.; Kurtz, S.; Kazmerski, L.; Steiner, M.; Gray, J.; Davenport, T.; Buelow, R.; Takacs, L.; Shatz, N.; Bortz, J.; Jani, O.; Goossen, K.; Kiamilev, F.; Doolittle, A.; Ferguson, I.; Unger, B.; Schmidt, G.; Christensen, E.; Salzman, D. *Prog. Photovolt: Res. Appl.* **2009**, *17*, 75.
- (15) Yu, P.; Chang, C. -H.; Chiu, C. -H.; Yang, C. -S.; Yu, J. -C.; Kuo, H. -C.; Hsu, S. -H.; Chang, Y. -C. *Adv. Mater.* **2009**, *21*, 1628.
- (16) Jackson, P.; Hariskos, D.; Lotter, E.; Paetel, S.; Wuerz, R.; Menner, R.; Wischmann, W.; Powalla, M. *Prog. Photovolt: Res. Appl.* **2011**, *19*, 894.
- (17) Gloeckler, M.; Sankin, I.; Zhao, Z. *IEEE J. Photovolt.* **2013**, *3*, 1389.
- (18) Green, M. A.; Emery, K.; Hishikawa, Y.; Warta, W.; Dunlop, E. D. *Prog. Photovolt: Res. Appl.* **2012**, *20*, 12.

- (19) Dong, Q.; Fang, Y.; Shao, Y.; Mulligan, P.; Qiu, J.; Cao, L.; Huang, J. *Science* **2015**, *347*, 967.
- (20) Ziang, X.; Shifeng, L.; Laixiang, Q.; Shuping, P.; Wei, W.; Yu, Y.; Li, Y.; Zhijian, C.; Shufeng, W.; Honglin, D.; Minghui, Y.; Qin, G. G. *Opt. Mater. Express* **2015**, *5*, 29.
- (21) Lin, Q.; Armin, A.; Nagiri, R. C. R.; Burn, P. L.; Meredith, P. *Nat. Photonics* **2015**, *9*, 106.
- (22) Miyata, A.; Mitioglu, A.; Plochocka, P.; Portugall, O.; Wang, J. T. -W.; Stranks, S. D.; Snaith, H. J.; Nicholas, R. J. *Nat. Phys.* **2015**, *11*, 582.
- (23) Ponceca, Jr., C. S.; Savenije, T. J.; Abdellah, M.; Zheng, K.; Yartsev, A.; Pascher, T.; Harlang, T.; Chabera, P.; Pullerits, T.; Stepanov, A.; Wolf, J. -P.; Sundström, V. *J. Am. Chem. Soc.* **2014**, *136*, 5189.
- (24) Yang, W. S.; Noh, J. H.; Jeon, N. J.; Kim, Y. C.; Ryu, S.; Seo, J.; Seok, S. I. *Science* **2015**, *348*, 1234.
- (25) Xing, G.; Mathews, N.; Sun, S.; Lim, S. S.; Lam, Y. M.; Grätzel, M.; Mhaisalkar, S.; Sum, T. C. *Science* **2013**, *342*, 344.
- (26) Ishihara, T. *J. Lumin.* **1994**, *60–61*, 269.
- (27) Koutselasy, I. B.; Ducassez, L.; Papavassiliou, G. C. *J. Phys.: Condens. Matter.* **1996**, *8*, 1217.
- (28) Tanaka, K.; Takahashi, T.; Ban, T.; Kondo, T.; Uchida, K.;

- Miura, N. *Solid State Commun.* **2003**, *127*, 619.
- (29) Hirasawa, M.; Ishihara, T.; Goto, T.; Uchida, K.; Miura, N. *Phys. B*, **1994**, *201*, 427.
- (30) Kim, H. -S.; Lee, C. -R.; Im, J. -H.; Lee, K. -B.; Moeh, T.; Marchioro, A.; Moon, S. -J.; Humphry-Baker, R.; Yum, J. -H.; Moser, J. E. *Sci. Rep.* **2012**, *2*, 591.
- (31) Lee, M. M.; Teuscher, J.; Miyasaka, T.; Murakami, T. N.; Snaith, H. J. *Science* **2012**, *338*, 643.
- (32) Liu, M.; Johnston, M. B.; Snaith, H. J. *Nature* **2013**, *501*, 395.
- (33) Jeon, N. J.; Noh, J. H.; Kim, Y. C.; Yang, W. S.; Ryu, S.; Seok, S. I. *Nat. Mater.* **2014**, *13*, 897.
- (34) Xiao, Z.; Dong, Q.; Bi, C.; Shao, Y.; Yuan, Y.; Huang, J. *Adv. Mater.* **2014**, *26*, 6503.
- (35) Burschka, J.; Pellet, N.; Moon, S. -J.; Humphry-Baker, R.; Gao, P.; Nazeeruddin, M. K.; Grätzel, M. *Nature* **2013**, *499*, 316.
- (36) Zhou, Z.; Pang, S.; Liu, Z.; Xu, H.; Cui, G. *J. Mater. Chem. A* **2015**, *3*, 19205.
- (37) Rostalski, J.; Meissner, D. *Sol. Energy Mater. Sol. Cells* **2000**, *61*, 87.
- (38) Kim, H.; Lim, K. -G.; Lee, T. -W. *Energy Environ. Sci.* **2016**, DOI: 10.1039/c5ee02194d.

- (39) Jeng, J. -Y.; Chiang, Y. -F.; Lee, M. -H.; Peng, S. -R.; Guo, T. -F.; Chen, P.; Wen, T. -C. *Adv. Mater.* **2013**, *25*, 3727.
- (40) Yeo, J. -S.; Kang, R.; Lee, S.; Jeon, Y. -J.; Myoung, N.; Lee, C. -L.; Kim, D. -Y.; Yun, J. -M.; Seo, Y. -H.; Kim, S. -S.; Na, S. -I. *Nano Energy* **2015**, *12*, 96.
- (41) Wang, K. -C.; Jeng, J. -Y.; Shen, P. -S.; Chang, Y. -C.; Diao, E. W. -G.; Tsai, C. -H.; Chao, T. -Y.; Hsu, H. -C.; Lin, P. -Y.; Chen, P.; Guo, T. -F.; Wen, T. -C. *Sci. Rep.* **2014**, *4*, 4756.
- (42) Ye, S.; Sun, W.; Li, Y.; Yan, W.; Peng, H.; Bian, Z.; Liu, Z.; Huang, C. *Nano Lett.* **2015**, *15*, 3723.
- (43) Wu, Z.; Bai, S.; Xiang, J.; Yuan, Z.; Yang, Y.; Cui, W.; Gao, X.; Liu, Z.; Jin, Y.; Sun, B. *Nanoscale* **2014**, *6*, 10505.
- (44) Chiang, C. -H.; Tseng, Z. -L.; Wu, C. -G. *J. Mater. Chem. A* **2014**, *2*, 15897.
- (45) Liu, X.; Yu, H.; Yan, L.; Dong, Q.; Wan, Q.; Zhou, Y.; Song, B.; Li, Y. *ACS Appl. Mater. Interfaces*, **2015**, *7*, 6230.
- (46) Liang, P. -W.; Chueh, C. -C.; Williams, S. T.; Jen, A. K. -Y. *Adv. Energy Mater.* **2015**, *5*, 1402321.
- (47) You, J.; Hong, Z.; Yang, Y.; Chen, Q.; Cai, M.; Song, T. -B.; Chen, C. -C.; Lu, S.; Liu, Y.; Zhou, H.; Yang, Y. *ACS Nano* **2014**, *8*, 1674.
- (48) Ryu, S.; Seo, J.; Shin, S. S.; Kim, Y. C.; Jeon, N. J.; Noh, J. H.;

- Seok, S. I. *J. Mater. Chem. A* **2015**, *3*, 3271.
- (49) Wei, P.; Oh, J. H.; Dong, G.; Bao, Z. *J. Am. Chem. Soc.* **2010**, *132*, 8852.
- (50) Wei, P.; Menke, T.; Naab, B. D.; Leo, K.; Riede, M.; Bao, Z. *J. Am. Chem. Soc.* **2012**, *134*, 3999.
- (51) Naab, B. D.; Guo, S.; Olthof, S.; Evans, E. G. B.; Wei, P.; Millhauser, G. L.; Kahn, A.; Barlow, S.; Marder, S. R.; Bao, Z. *J. Am. Chem. Soc.* **2013**, *135*, 15018.
- (52) Cho, N.; Yip, H. -L.; Davies, J. A.; Kazarinoff, P. D.; Zeigler, D. F.; Durban, M. M.; Segawa, Y.; O'Malley, K. M.; Luscombe, C. K.; Jen, A. K. -Y. *Adv. Energy Mater.* **2011**, *1*, 1148.
- (53) Li, H.; Fu, K.; Hagfeldt, A.; Grätzel, M.; Mhaisalkar, S. G.; Grimsdale, A. C. *Angew. Chem. Int. Ed.* **2014**, *53*, 4085.
- (54) Jeon, N. J.; Lee, J.; Noh, J. H.; Nazeeruddin, M. K.; Grätzel, M.; Seok, S. I. *J. Am. Chem. Soc.* **2013**, *135*, 19087.
- (55) Wang, J.; Wang, S.; Li, X.; Zhu, L.; Meng, Q.; Xiao, Y.; Li, D. *Chem. Commun.* **2014**, *50*, 5829.
- (56) Lv, S.; Han, L.; Xiao, J.; Zhu, L.; Shi, J.; Wei, H.; Xu, Y.; Dong, J.; Xu, X.; Li, D.; Wang, S.; Luo, Y.; Meng, Q.; Li, X. *Chem. Commun.* **2014**, *50*, 6931.
- (57) Christians, J. A.; Fung, R. C. M.; Kamat, P. V. *J. Am. Chem. Soc.* **2014**, *136*, 758.

- (58) Heo, J. H.; Im, S. H.; Noh, J. H.; Mandal, T. N.; Lim, C. -S.; Chang, J. A.; Lee, Y. H.; Kim, H.; Sarkar, A.; Nazeeruddin, M. K.; Grätzel, M.; Seok, S. I. *Nat. Photonics* **2013**, *7*, 486.
- (59) Qin, P.; Peak, S.; Dar, M. I.; Pellet, N.; Ko, J.; Grätzel, M.; Nazeeruddin, M. K. *J. Am. Chem. Soc.* **2014**, *136*, 8516.
- (60) Yu, Z.; Sun, L. *Adv. Energy Mater.* **2015**, *5*, 1500213.
- (61) Liu, Y.; Hong, Z.; Chen, Q.; Chen, H.; Chang, W. -H.; Yang, Y. (M.); Song, T. -B.; Yang, Y. *Adv. Mater.* **2015**, DOI: 10.1002/adma.201504293.
- (62) Lin, Y.; Zhan, X. *Mater. Horiz.* **2014**, *1*, 470.
- (63) Zang, Y.; Li, C. -Z.; Chueh, C. -C.; Williams, S. T.; Jiang, W.; Wang, Z. -H.; Yu, J. -S.; Jen, A. K. -Y. *Adv. Mater.* **2014**, *26*, 5708.
- (64) Jung, I. H.; Zhao, D.; Jang, J.; Chen, W.; Landry, E. S.; Lu, L.; Talapin, D. V.; Yu, L. *Chem. Mater.* **2015**, *27*, 5941.
- (65) Hwang, Y. -J.; Earmme, T.; Courtright, B. A. E.; Eberle, F. N.; Jenekhe, S. A. *J. Am. Chem. Soc.* **2015**, *137*, 4424.
- (66) Hwang, Y. -J.; Courtright, B. A. E.; Ferreira, A. S.; Tolbert, S. H.; Jenekhe, S. A. *Adv. Mater.* **2015**, *27*, 4578.
- (67) Lin, Y.; Zhang, Z. -G.; Bai, H.; Wang, J.; Yao, Y.; Li, Y.; Zhu, D.; Zhan, X. *Energy Environ. Sci.* **2015**, *8*, 610.
- (68) Facchetti, A. *Mater. Today* **2013**, *16*, 123.

- (69) Sonar, P.; Lim, J. P. F.; Chan, K. L. *Energy Environ. Sci.* **2011**, *4*, 1558.
- (70) Eftaiha, A. F.; Sun, J. -P.; Hill, I. G.; Welch, G. C. *J. Mater. Chem. A* **2014**, *2*, 1201.
- (71) Zhan, X.; Tan, Z. A.; Domercq, B.; An, Z.; Zhang, X.; Barlow, S.; Li, Y.; Zhu, D.; Kippelen, B.; Marder, S. R. *J. Am. Chem. Soc.* **2007**, *129*, 7246.
- (72) Nielsen, C. B.; Holliday, S.; Chen, H. -Y.; Cryer, S. J.; McCulloch, I. *Acc. Chem. Res.* **2015**, *48*, 2803.
- (73) Sun, D.; Meng, D.; Cai, Y.; Fan, B.; Li, Y.; Jiang, W.; Huo, L.; Sun, Y.; Wang, Z. *J. Am. Chem. Soc.* **2015**, *137*, 11156.
- (74) Heo, J. H.; Han, H. J.; Kim, D.; Ahn, T. K.; Im, S. H. *Energy Environ. Sci.* **2015**, *8*, 1602.
- (75) Chen, Q.; Zhou, H.; Hong, Z.; Luo, S.; Duan, H. -S.; Wang, H. -H.; Liu, Y.; Li, G.; Yang, Y. *J. Am. Chem. Soc.* **2014**, *136*, 622.
- (76) Tsai, H.; Nie, W.; Cheruku, P.; Mack, N. H.; Xu, P.; Gupta, G.; Mohite, A. D.; Wang, H. -L. *Chem. Mater.* **2015**, *27*, 5570.
- (77) Bi, D.; Yang, L.; Boschloo, G.; Hagfeldt, A.; Johansson, E. M. J. *J. Phys. Chem. Lett.* **2013**, *4*, 1532.
- (78) Li, J.-F.; Zhang, Z.-L.; Gao, H.-P.; Zhang, Y.; Mao, Y.-L. *J. Mater. Chem. A* **2015**, *3*, 19476.
- (79) Zhang, W.; Saliba, M.; Moore, D. T.; Pathak, S. K.; Hörantner,

- M. T.; Stergiopoulos, T.; Stranks, S. D.; Eperon, G. E.; Alexander-Webber, J. A.; Abate, A.; Sadhanala, A.; Yao, S.; Chen, Y.; Friend, R. H.; Estroff, L. A.; Wiesner, U.; Snaith, H. *J. Nat. Commun.* **2015**, *6*, 6142.
- (80) Chen, B.; Zheng, X.; Yang, M.; Zhou, Y.; Kundu, S.; Shi, J.; Zhu, K.; Priya, S. *Nano Energy* **2015**, *13*, 582.
- (81) Luo, P.; Liu, Z.; Xia, W.; Yuan, C.; Cheng, J.; Lu, Y. *ACS Appl. Mater. Interfaces* **2015**, *7*, 2708.
- (82) Guldi, D. M.; Hungerbuhler, H.; Janata, E.; Asmus, K. -D. *J. Phys. Chem.* **1993**, *97*, 11258.
- (83) Seo, J.; Park, S.; Kim, Y. C.; Jeon, N. J.; Noh, J. H.; Yoon, S. C.; Seok, S. I. *Energy Environ. Sci.* **2014**, *7*, 2642.
- (84) Wang, J. C.; Ren, X. C.; Shi, S. Q.; Leung, C. W.; Chan, P. K. *L. Org. Electron.* **2011**, *12*, 880.
- (85) Xu, Y.; Zhu, L.; Shi, J.; Lv, S.; Xu, X.; Xiao, J.; Dong, J.; Wu, H.; Luo, Y.; Li, D.; Meng, Q. *ACS Appl. Mater. Interfaces* **2015**, *7*, 2242.
- (86) Kim, S. S.; Bae, S.; Jo, W. H. *Chem. Commun.* **2015**, *51*, 17413.
- (87) Jiao, Y.; Liu, K.; Wang, G.; Wang, Y.; Zhang, X. *Chem. Sci.*, **2015**, *6*, 3975.
- (88) Huang, C.; Sartin, M. M.; Siegel, N.; Cozzuol, M.; Zhang, Y.; Hales, J. M.; Barlow, S.; Perry, J. W.; Marder, S. R. *J. Mater.*

Chem. **2011**, *21*, 16119.

- (89) Wu, B.; Fu, K.; Yantara, N.; Xing, G.; Sun, S.; Sum, T. C.; Mathews, N. *Adv. Energy Mater.* **2015**, *5*, 1500829.

초 록

유무기 복합 페로브스카이트 물질은 긴 자유전하이동거리와 빠른 전하이동속도, 낮은 여기자의 결합 에너지 및 높은 흡광 계수 등의 고유한 장점들로 인하여 차세대 고성능 태양전지의 광활성층 물질로서 활발히 연구되고 있다. 게다가 유무기 복합 페로브스카이트는 그 박막 제조 방법이 비교적 간단하고, 전구체 물질의 가격 또한 저렴한 장점을 가지고 있다. 이러한 장점들을 가진 유무기 복합 페르브스카이트 기반의 태양전지는 최근 빠르게 발전하여 짧은 연구 역사에도 불구하고 이미 20% 이상의 태양전지 효율을 기록하였다.

‘ITO/PEDOT:PSS/유무기 복합 페로브스카이트($\text{CH}_3\text{NH}_3\text{PbI}_3$)/전자 수송층/알루미늄’의 구조를 갖는 inverted 평면이종접합 페로브스카이트 태양전지는 저온 공정과 용액 공정이 가능하다는 장점을 가지고 있어 많은 관심을 모으고 있다. 이 구조에서 전자 수송층 물질로는 C_{60} , PCBM, PC_{71}BM , ICBA 등과 같은 풀러렌 유도체들이 주로 사용되는데 이는 풀러렌 유도체들이 상온에서 높은 용해도를 가지며, 페로브스카이트 층에 악영향을 끼치지 않는 용액공정이 가능하기 때문이다.

최근 유기 태양전지 분야에서는 풀러렌 유도체들에 비해 높은 가시광선 영역의 빛 흡수, 튜닝이 용이한 에너지 레벨, 저가 공정 등의 장점을 가지는 비풀러렌 전자받개 물질들이 많이 연구되고 있다. 하지만, 이를 페로브스카이트 태양전지의 전자 수송층 물질로

사용하기 위해서는 보다 높은 전기전도도와 전자이동도가 갖춰져야만 한다. 그 이유는 inverted 구조를 갖는 페로브스카이트 태양전지의 경우, 페로브스카이트 층과 금속 양극이 직접 맞닿는 현상을 방지하기 위해 충분한 두께의 전자 수송층을 코팅해야 하기 때문이다.

1,3-Dimethyl-2-phenyl-2,3-dihydro-1*H*-benzimidazole (DMBI) 라는 물질은 풀러렌이나 naphthalene diimide 유도체 등과 같은 *n*-type 물질들의 전기적 특성을 강화하기 위한 *n*-type 도펀트로 수 차례 보고된 바 있다. DMBI는 일반적인 유기 용매에 대한 용해도가 좋기 때문에 *n*-type 물질들과 섞어 유기 용매에 녹임으로써 간단하게 도핑을 시킬 수 있다. DMBI는 페로브스카이트 태양전지의 전자 수송층으로 쓰일 물질들을 효과적으로 *n*-도핑시킬 수 있을 것이기에 태양전지 효율의 향상을 기대해볼 수 있다.

본 연구에서는 평면이종접합 구조를 갖는 페로브스카이트 태양전지의 전자 수송층 물질로 쓰일 *n*-type 물질들 (PCBM, perylene diimide (PDI) 기반의 저분자 물질들)에 대한 *n*-도핑 효과를 연구하였다. 그 결과 소량의 DMBI만으로도 전자 수송층 물질들을 효과적으로 *n*-도핑할 수 있다는 것이 페르미 레벨의 상승으로 증명되었다. 게다가, 전자 수송층 물질들의 전기 전도도가 *n*-도핑으로 인해 대폭 상승함으로 인해 전류밀도를 비롯한 태양전지 효율이 크게 증가하였다. 또한 photoluminescence 실험을 통하여 PDI 기반의 diPDI 물질이 PCBM을 상회하는 전자받개로서의 성능을 나타냄을 보여주었다.

주요어: 페로브스카이트 태양전지, 평면 이중접합, inverted 구조, n -도핑, 전자 수송층, 전하 이동, 전기전도도, 비폴러렌 전자받개

학 번: 2010-24052